# Dynamic Particle Rejection on Optical Lenses Using Piezoelectric Elements

By

Scott Cravens

Submitted to the graduate degree program in Aerospace Engineering and the Graduate Faculty of the University of Kansas in partial fulfillment of the requirements for the degree of Master of Science

_____

Chairperson Dr. Ronald Barrett

_____

Dr. Mark Ewing

_____

Dr. Craig McLaughlin

Date approved:

The Thesis Committee for Scott Cravens

certifies that this is the approved version of the following thesis:

**Dynamic Particle Rejection on Optical Lenses Using Piezoelectric Elements**

_____

Chairperson Dr. Ronald Barrett

_____

Dr. Mark Ewing

_____

Dr. Craig McLaughlin

Date approved:

## Abstract

In the present investigation, the potential for removing undesirable particles from optical surfaces remotely has been explored. The primary target for this research is in surveillance cameras, satellite lenses, planetary rover optical lenses and other space based optical systems. The mechanism for removing these particles is dynamic vibrations of the optical lens wherein natural modes are excited which results in accelerations on the lenses surface that are sufficiently high to reject the particle.

The following sections will progress through a discussion on the need for a system which can remove particles from optical surfaces followed by an examination of current techniques for particle removal from semiconductor surfaces, comparisons of current theory for the adhesion of particles to surfaces, as well as patents which deal with removing dust particles from digital single reflex cameras. Following this, scientific theory employed for this investigation will be presented. The theory is centered on particle adhesion phenomena and forces, as well as the dynamic response of flat plates to vibration. The experimental apparatus used for this investigation will also be explained along with the procedures employed during the research.

This paper will conclude by presenting the results of the investigation. It was found that for the experimental device used, glass microspheres with a diameter larger than 80 μm could be rejected from a glass surface using 8600 Hz dynamic vibrations. The surface acceleration measured at this frequency was 150 m/sec$^2$ (15 g) determined using a Polytech laser vibrometer. By using an impinging flow of air at a velocity of 3.5 m/s, particles with diameters greater than 40 μm were able to be dislodged. By using a combination of dynamic vibrations and blowing air, glass microspheres with diameters greater than 5 μm were successfully removed from the surface. The theoretical adhesion force for an 80 μm glass microsphere is approximately 7 μN and is composed of Van der Waals and electrostatic forces. The observed adhesion force was 5 nN, three orders of magnitude less than predicted. This discrepancy is attributed to surface roughness and particle to particle interactions.

## Acknowledgments

There are a number of people who are due thanks for their assistance in this endeavor. First and foremost, I would like to thank Dr. Ron Barrett for his never ending patience and guidance throughout my graduate career, as well as this thesis. Additional thanks are due to Dr. Mark Ewing for his freely given assistance throughout this project as well as for sitting on my committee. I would also like to thank Dr. Craig McLaughlin for sitting on my committee. The University of Kansas Department of Aerospace Engineering as a whole is also due a great debt of gratitude. Additional thanks goes to the Transportation Research Institute for their support of the project

Thanks are also due to Wes Ellison. Without his expertise with electronics this project would not have succeeded. I would also like to thank Richard Bramlette and Mike Brennison for their freely given advice and help in working through problems. Akhilesh Katipally and Saiarun Kolapan Jayachandran are also due thanks for their assistance.

Special thanks are given to my family and Kodi Caster for their incredible patience and encouragement. My work pace and attention span can be exceptionally frustrating at times. For their unwavering support over the past few years I am truly grateful.

# Table of Contents

**Page No.**

*Table of Contents (continued)*

**Page No.**

## List of Symbols

| Symbol | Description | Units |
|---|---|---|
| $a$ | acceleration | $m/s^2$ |
| $a_{dl}$ | double layer force removal acceleration | $m/s^2$ |
| $a_{imag}$ | image force removal acceleration | $m/s^2$ |
| $a_{vdw}$ | Van der Waals force removal acceleration | $m/s^2$ |
| $A$ | Hamaker constant | eV, J |
| | plate coefficient | ~ |
| $C$ | capacitance | Coulomb/Volt |
| $d$ | diameter | m |
| $D$ | dielectric constant | ~ |
| $D_E$ | flexural rigidity | N·m |
| $E$ | elastic modulus | $N/m^2$ |
| $f$ | frequency | Hz |
| $F$ | force | N |
| $F_{adh}$ | adhesive force | N |
| $F_{dl}$ | double layer force | N |
| $F_D$ | drag force | N |
| $F_f$ | friction force | N |
| $F_{imag}$ | image force | N |

***List of Symbols (continued)***

| **Symbol** | **Description** | **Units** |
|---|---|---|
| $F_{vdw}$ | Van der Waals force | N |
| h | Lifshitz Van der Waals constant | eV |
| | plate thickness | m |
| $l$ | distance | m |
| P | power | W |
| q | electric charge | Coulomb |
| r | radius | m |
| R | radius | m |
| Re | Reynolds number | ~ |
| S | scale factor | ~ |
| u | velocity | m/s |
| $u_{max}$ | maximum velocity | m/s |
| $u_{rms}$ | root mean squared velocity | m/s |
| U | electrical potential | Volt |
| t | time | sec |
| T | temporal function | ~ |
| w | displacement | m |
| x | spatial coordinate | m |

***List of Symbols (continued)***

| Symbol | Description | Units |
|---|---|---|
| X | spatial function | ~ |
| y | spatial coordinate | m |
| Y | spatial function | ~ |
| z | separation distance | m |

| Greek Symbol | Description | Units |
|---|---|---|
| $\alpha$ | plate equation constant | rad/m |
| $\beta$ | plate equation constant | rad/m |
| $\varepsilon_o$ | permittivity of free space | C/V |
| $\gamma$ | plate equation constant | rad/m |
| $\mu$ | dynamic viscosity | $N \cdot s/m^2$ |
| $\mu_{sf}$ | coefficient of static friction | ~ |
| $\rho$ | density | $kg/m^3$ |
| $\omega$ | frequency | rad/s |

*List of Symbols (continued)*

| **Subscript** | **Description** |
|---|---|
| adh | adhesive |
| air | air |
| dl | double layer |
| D | drag |
| int | inertia |
| imag | image |
| L | lift |
| max | maximum |
| pt | particle |
| rms | root mean square |
| sf | static friction |
| surf | surface |
| t | differentiation with respect to time |
| vac | vacuum |
| vdw | Van der Waals |
| w | weight |

## List of Figures

**Page No.**

*List of Figures (continued)*

**Page No.**

## List of Tables

**Page No.**

# 1. Introduction

Atmospheric dust particles are easily deposited on airborne surveillance equipment, ground based static surveillance equipment and hand held camera lenses. For the most part these particles, if large enough in size to adversely affect image quality, are easily removed by whoever is operating the equipment. However, for surveillance systems that are not easily reached, or satellites in orbit, and even extra-planetary rovers or telescopes, once a dust particle has settled onto the view frame it is likely to remain there indefinitely. The goal of this research is to develop a method whereby undesirable particle deposits can be removed remotely from an optical lens using high frequency vibrations. The following sections will explain current technology for particle rejection from planar surfaces, as well as a patented method for dynamic removal of dust particles inside of a digital camera.

## 1.1 Purpose

Particulates fouling a lens or filter block and scatter light which would otherwise pass through the lens[1]. A particle can also interfere with an image by scattering light into the lens creating undesirable bright spots [1]. The extent to which the resulting image is affected is dependent on several factors including the aperture settings of the camera, the focal length of the camera as well as the distance between the camera and the object of interest. All of these factors will vary from one application to the next and will determine the minimum size of a dust particle that could impact the image.

One example of where particles were of concern is the Mars Exploration Rover (MER) Descent Image Motion Estimation System (DIMES)[2]. The purpose of this system was to estimate the horizontal wind velocity of a descending lander by comparing stationary points in three images taken during descent. Ref. 2 investigated the effect of dust particles, which could appear as stationary geographic features, on this system by artificially inserting image artifacts into the algorithm used to calculate the wind velocity. The size of the artificial dust particles ranged from 0.1 to 0.25 mm in diameter and the findings showed that a particle count of 1 to 2 would

not have an impact on the accuracy of the calculations. However, if there were more particles than this the algorithm could be compromised. Figure 1.1 shows the type of image artifact which could interfere with the MER DIMES accuracy. The image was taken looking down at the ground from a helicopter during a test flight.

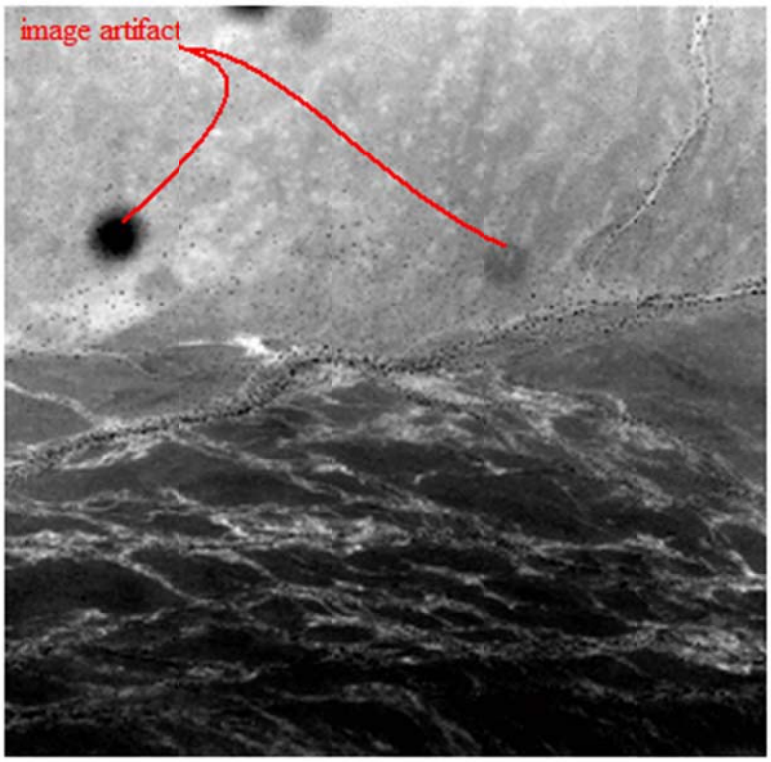


**Figure 1.1: MER DIMES Image Artifact**[2]

An additional system on the MER rover which could be adversely affected by dust was the stereo cameras used to locate hazards while the rover was driving. It was determined that particles with a diameter less than 45 μm would not interfere with the operation of this system, and fortunately during operation of the rover larger particles were not often encountered.

For the Mars rover, a simple integrated system which could remove dust particles while not adding significant weight to the rover would be advantageous. Such a system would be useful

on a lunar mission as well. Another aspect of such a device that would be useful is that even if it were possible to physically wipe particles from a lens, doing so could permanently damage the lens by scratching it. This is especially likely for a device on the moon where the particles are so abrasive that they wore through the outer layer of the Apollo astronauts' gloves[3]. The cameras used by the astronauts also suffered from dust on the lens which was simply tolerated instead of being wiped free[3].

In a paper entitled *Adhesion of Lunar Dust*[4], the need for a system to remove lunar dust is further described. The author explains that a very dilute layer of levitated fine charged particles is likely in motion above the surface which will deposit on any surface encountered. These particles are driven to motion not by atmospheric forces, but by static electric effects such as UV photo-ionization. The particles are lunar regolith which is a mixture of dust and rocky debris caused by meteor impacts on the moon, with the majority of particle diameters ranging from 40 to 130 μm and a density of 1.5 g/cm$^3$. Ref. 4 describes the lunar regolith as being somewhat elongated and angular to sub-angular due to the lack of air and water on the moon which would otherwise have caused weathering of the particles.

As an example of particles blocking light transmission through a lens filter, Figure 1.2 shows glass microspheres with diameters ranging from 15 to 150 μm which have been deposited on a lens filter. The glass microspheres are held to the surface by electrostatic and Van der Waals forces. Figure 1.3 shows the loss of detail in the graph paper which was used as a backdrop. This example is severe, and is unlikely to be representative of installed cameras, but it does serve to show the potential for problems arising from blowing debris.

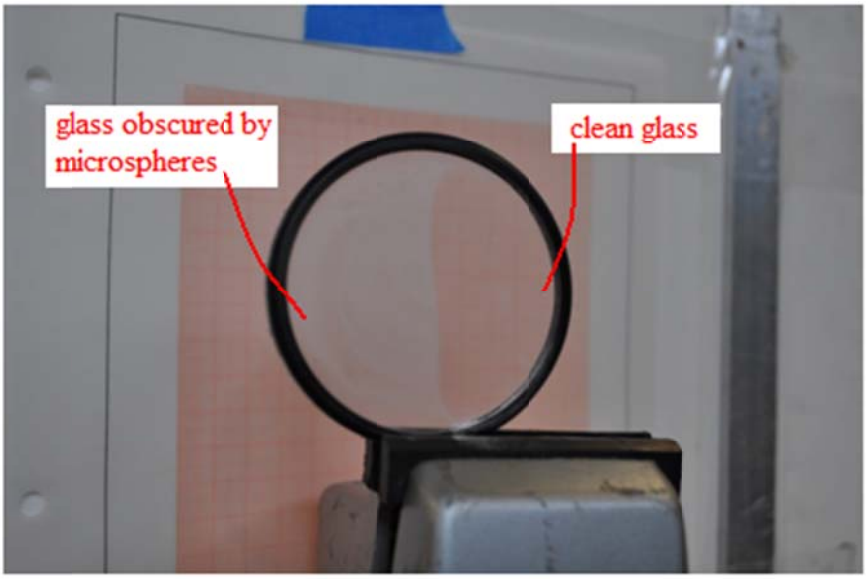


**Figure 1.2: UV Filter with Deposited Glass Microspheres**


**Figure 1.3: Graph Paper Obscured by Glass Microspheres**

## 1.2 Previous Commercial Technologies

Perhaps the most relevant application where particle removal is of importance is found in the manufacturing of semiconductors. To facilitate the decreasing size of electronics, circuits printed on semi-conductors must follow suit. These circuits are small enough that a particle with a diameter less than 1 μm is capable of rendering the circuit useless[5]. For this reason a large body of research has been conducted to understand the forces involved in the adhesion of a particle to a surface.

Researchers who are mainly concerned with the adhesion of particles on silicon semi-conductors develop their theory of adhesion forces independent of application which makes their research ideal for estimating the force of adhesion for particles on a glass optical lens. The development of the theoretical adhesion forces used for this thesis is obtained from References 5 through 15. All of these papers agree on the basic types of forces which work to adhere a particle to a surface. These forces are the surface energy Van der Waals forces and the electrostatic image and double layer forces. There is some variation in the form of the equations presented in the literature, but they are fundamentally equivalent (depending on various assumptions considered by the different authors).

Among the literature, a common point which is discussed is the accuracy of the theoretical equations with respect to experimental evidence. Ref. 10 and Ref. 7 suggest that two orders of magnitude difference between experimental data and theoretical predictions is typical, with the experimentally determined force being less than the theoretical. This disparity in adhesion force magnitude is commonly attributed to surface irregularities, which will reduce the Van der Waals forces. Another cause of lower adhesion forces with respect to electrostatic forces is the difficulty of measuring the charge on particles. To account for this the charge is often assumed to be at a maximum value which is often not the case

There are several methods for removing particles from surfaces including centrifugal acceleration, aerodynamic/hydrodynamic effects, and vibration. For the purposes of this research, centrifugal acceleration is not an option because the goal is to develop a system to clean particles from a fixed camera lens. Hydrodynamic methods alone are also undesirable because they involve submerging the article to be cleaned in a fluid bath and directing high frequency ($10^3$ to $10^6$ Hz) acoustic waves at the surface. These waves can be either normal to the surface or parallel to it.

The two most promising methods for remotely removing particles are aerodynamic and vibrational methods. An aerodynamic removal method would consist of blowing a gas across the surface to remove the particles through drag forces. Ref. 4 suggests this method would be a viable option for large particles, but that micron sized particles could be lost within the boundary layer of the gas flow along the surface. This method is also not terribly practical for a satellite because a supply of gas would have to be added to the mission weight which is prohibitively expensive. However, Ref. 4 suggests that $CO_2$ gas and liquid is readily available on Mars, and has been vented from space based environments like the International Space Station in the past. The use of $CO_2$ gas for removing particles has been considered by NASA as a viable method[4].

Using vibrational energy to remove particles from an optical lens is an attractive option due to the possibility of integrating a shaking device into the housing of a camera. This method has been used to measure adhesion forces and so should lend itself well to removal applications. Vibrating the surface in a direction normal to its plane will incite an inertial force to the particle that is proportional to the particle radius cubed[5]. Van der Waals forces and double layer forces scale linearly with the radius of the particle, and the image force scales with the square of the particles radius. This means that the required acceleration for removal of the particles is inversely proportional to the radius of the particle as the radius increases, but will increase without bound as the radius approaches zero.

Using structural vibrations for dust removal is currently in use in the digital camera industry. Many digital single reflex (DSLR) cameras have a built in cleaning function which vibrates a filter inside of the camera to shake dust particles loose[16]. Olympus Optical Co. holds several patents[17,18] for a dust removal mechanism which utilizes piezoelectric elements bonded to a glass filter. The piezoelectric elements excite bending vibrations in the filter to remove dust particles. A significant difference between this device, shown in Figure 1.4 and Figure 1.5 lies in the location of the cleaning mechanism. The Olympus mechanism is located inside the body of the camera between the optical sensor and the lens of the camera, whereas the goal of this thesis is to remove particles from the outer face of a lens.

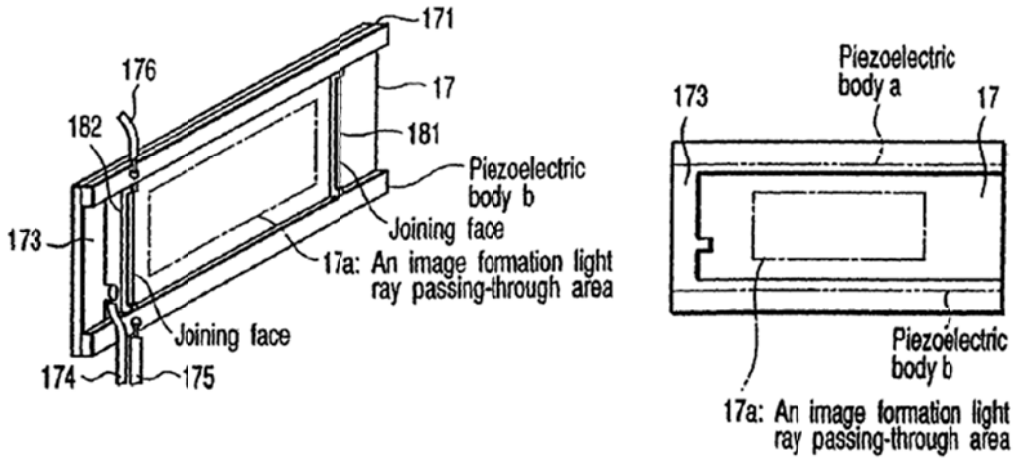


**Figure 1.4: Olympus Dust Removal Mechanism[18]**

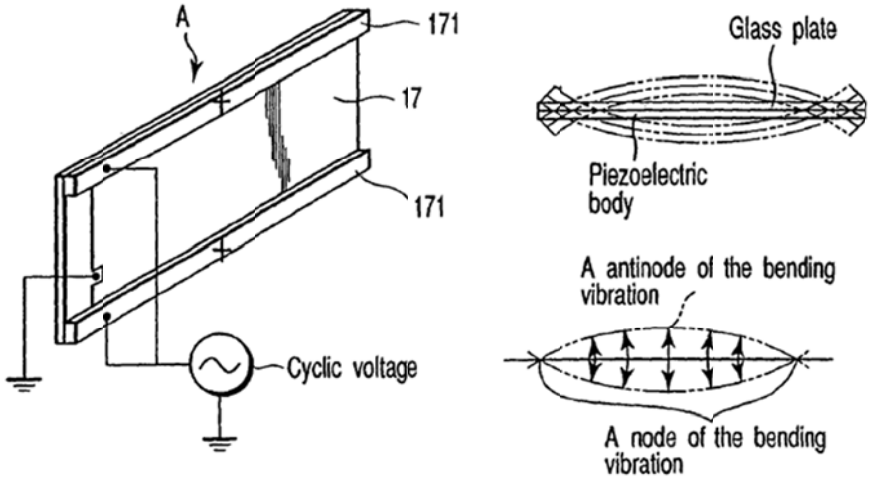


**Figure 1.5: Olympus Dust Removal Mechanism Operation[18]**

## 1.3 Previous Filament Cleaning Technologies

The current investigation is an extension of a previous work[19] relating to dynamic cleaning of filaments. In this investigation, 5-30 μm diameter particles were distributed on the sensing wire of the hot wire anemometer shown in Figure 1.6. To remove the particles, a piezoelectric actuator was integrated into the support structure of the anemometer to incite transverse vibrations of the sensing wire. This assembly is shown in Figure 1.7.

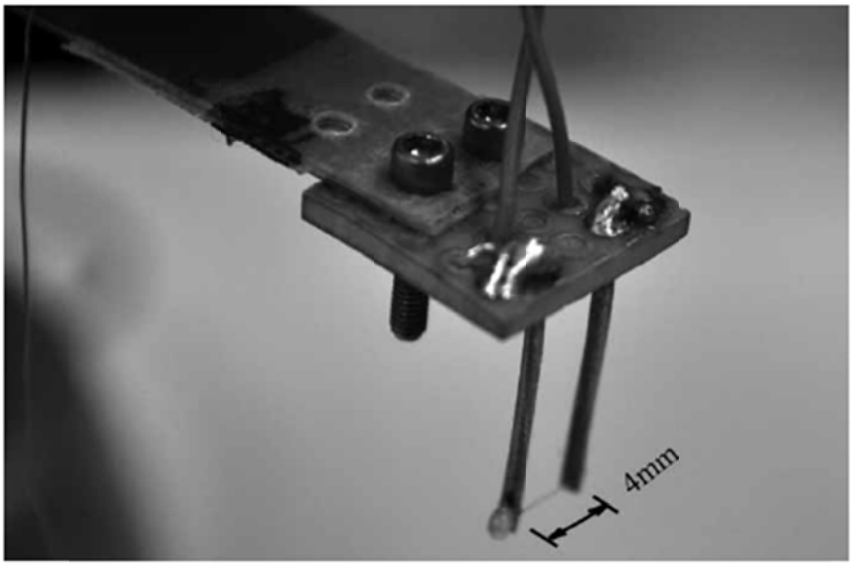


**Figure 1.6: Anemometer[19]**

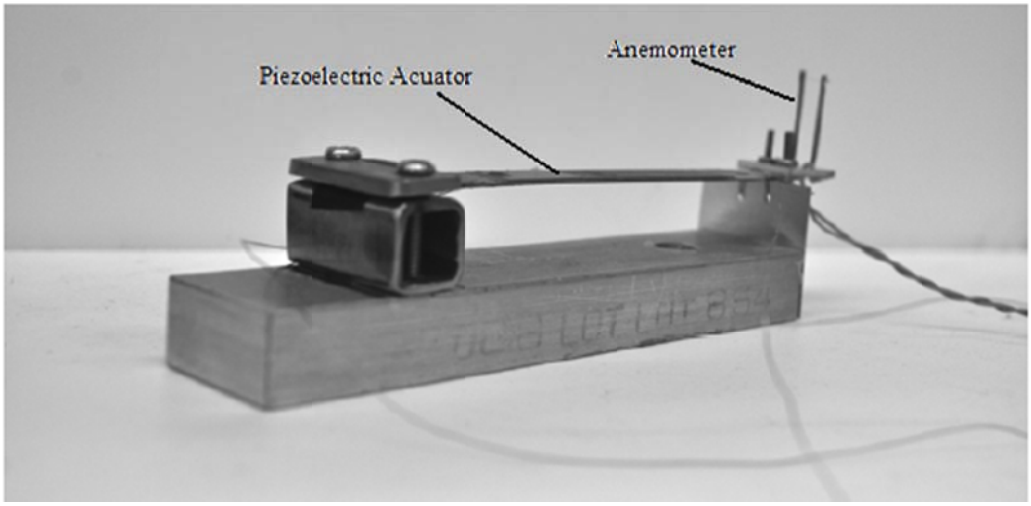


**Figure 1.7: Anemometer Cleaning Device[19]**

Figure 1.8 shows the results of this research. The curves in the figure represent the current flowing through the sensing wire of the anemometer as a 4 m/s airflow is cycled over it, with the peaks indicating zero airspeed. Figure 1.9 shows the condition of the wire for the respective curve in Figure 1.8. The dusted curve shows that the particles cause erratic behavior of the anemometer which renders the device unreliable. By inciting vibrations on the sensing wire, however, the particles are successfully removed and the performance of the anemometer is restored.

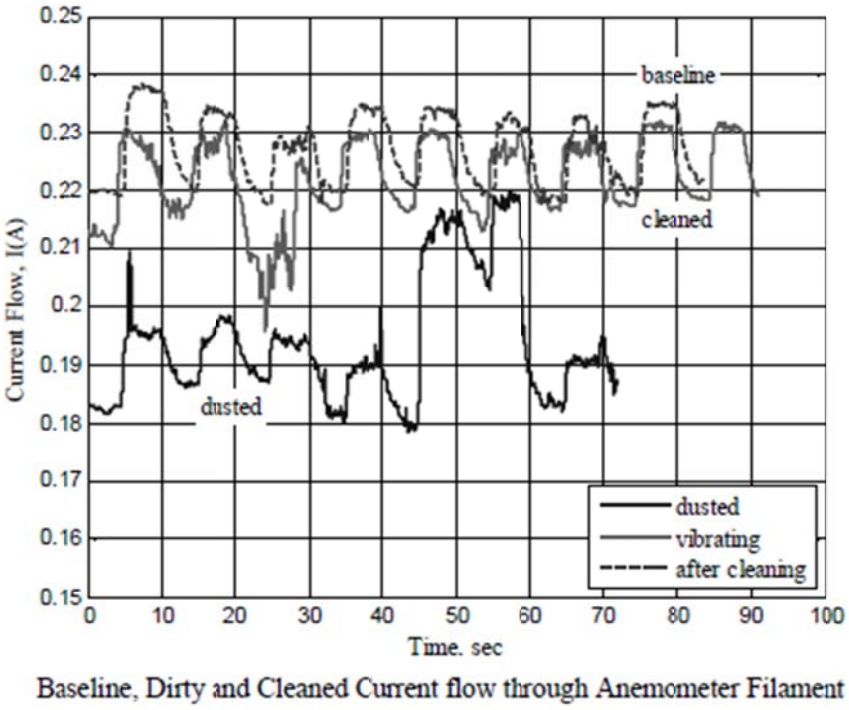


**Figure 1.8: Dynamically Cleaned Anemometer Performance[19]**

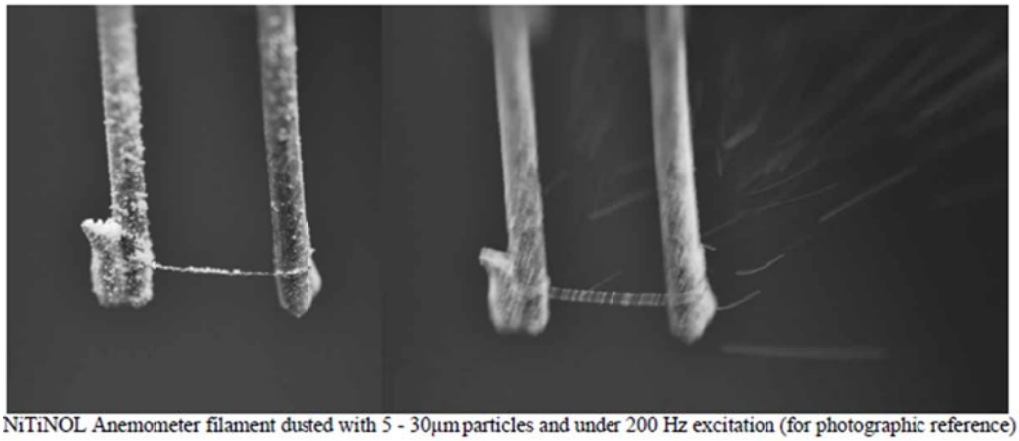

NiTiNOL Anemometer filament dusted with 5 - 30μm particles and under 200 Hz excitation (for photographic reference)

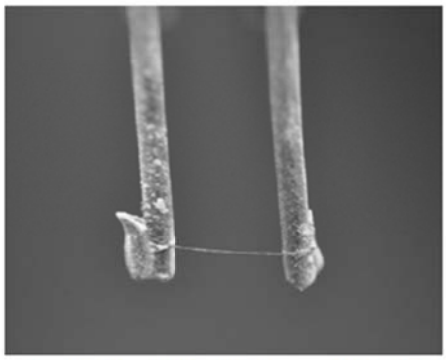

Anemometer after Cleaning with Infra-through Ultrasonic Vibrations

**Figure 1.9: Dynamic Cleaning of Hot Wire Anemometer[19]**

## 2. Theory and General Design

Adhesion forces on particles are difficult to predict and are dependent on several variables. The following sections will discuss methods of predicting these adhesion forces and the design of a system to counteract these forces to remove particles.

### 2.1 Adhesion Forces

The primary forces which act to adhere particles to a dry surface are Van der Waals forces and electrostatic forces. Van der Waals forces can be classified as dipole-dipole forces, induced-dipole dipole forces and dispersion forces[5]. Dispersion forces arise from the unsymmetrical distribution of electrons in neighboring atoms. When two molecules approach each other, the electron cloud surrounding each molecule repels the electrons surrounding the other causing an induced dipole condition. According to Ref. 5, these dispersion forces are the most important type of Van der Waals forces. Electrostatic forces that influence particles include electrostatic image forces and double layer forces[6].

#### 2.1.1 Van der Waals forces

A detailed discussion of the underlying physics of Van der Waals forces is beyond the scope of this paper. It is, however, informative to explore the simplified theory for predicting Van der Waals forces to gain an understanding of a particles interaction with a surface. For an in depth discussion of Van der Waals forces, the interested reader is referred to References 7 and 10.

A simple relation for predicting the Van der Waals force between two particles is given by Equations 1 and 2[10]. If the second particles radius is allowed to grow very large with respect to the first, i.e. approaching a planar surface, then Eq. 1 reduces to Eq. 2.

$$F_{vdw} = \frac{A}{6z^2}\frac{R_1 R_2}{R_1 + R_2} \quad (1)$$

$$F_{vdw} = \frac{AR}{6z^2} \quad (2)$$

The constant A is known as the Hamaker constant and is material dependent, z is the separation distance and R is the particle radius. The Hamaker constant is often difficult to measure experimentally, but Ref. 5 suggests that a typical value is on the order of 100 zJ. Table 2.1 gives some empirically determined Hamaker constants obtained from Ref. 6. Unless otherwise noted, the Hamaker constant is assumed to be 100 zJ. The separation distance, z, also has a generally assumed value of 4 Å[5,6,10]. This value is chosen as the contact limit and is approximately equal to the molecular diameter of the particle's constituent atoms[10].

Equations 1 and 2 assume a perfectly spherical particle to simplify the calculations. This is rarely the case in nature with real particles having irregular shapes and rough surfaces. These two factors tend to reduce the Van der Waals force between the particle and surface by increasing the limit of contact.

**Table 2.1: Hamaker Constants[6]**

| Particle | Surface | Hamaker Constant | |
|---|---|---|---|
| | | A (eV) | A (zJ) |
| polymer | polymer | 0.14-0.21 | 23-34 |
| KBr | KBr | 0.48 | 76 |
| $Al_2O_3$ | $Al_2O_3$ | 0.95 | 153 |
| Ge | Ge | 1.6-1.8 | 252-291 |
| Si | Si | 1.6-1.7 | 260-275 |
| Ge | Si | 1.8 | 287 |
| graphite | graphite | 1.7 | 275 |
| graphite | Si | 1.6 | 260 |
| Cu | Cu | 2.0 | 325 |
| Ag | Ag | 2.2 | 344 |

The Hamaker constant is not actually constant and tends to decrease with increasing separation distance[5]. According to Ref. 5, theoretical calculations of Hamaker constants often do not match up with those obtained experimentally and advises that the Hamaker constant is an adjustable parameter describing adhesion phenomena. With this in mind, the values of the Hamaker constant in Table 2.1 were calculated using the Lifshitz-Van der Waals constant, h, which Bowling suggests is a more reliable material property[6]. The Hamaker constant that Ref. 5 suggests using, A=100 zJ, is on the same order of magnitude as the constants given by References 6 and 10.

The Van der Waals force equation which Ref. 6 suggests using is given below. The Lifshitz Van der Waals constant, h, has units of eV and the radius, r, has units of meters.

$$F_{vdw} = \frac{hr}{8\pi z^2} \tag{3}$$

This expression is equivalent to Eq. 2 by equating the Hamaker constant, A, to the Lifshitz-Van der Waals constant.

$$h = \frac{4\pi A}{3} \tag{4}$$

The Lifshitz-Van der Waals constant has values ranging from about 0.6 eV to 9 eV[6]. Ref. 6 simplifies this equation for the Van der Waals force as follows by assuming z = 4 Å where the diameter, d, is in microns.

$$F_{vdw} = 2 \times 10^{-8} hd \quad N \tag{5}$$

### 2.1.2 Electrostatic Forces

The two primary electrostatic forces are electrostatic image force and contact potential double layer forces. The double layer force is a result of differing molecular energy states in two different materials in contact[6]. When these materials come into contact, a potential difference, U, is generated due to the transfer of electrons between the two materials. This potential difference ranges in value from 0 to 0.5 V[6]. The equation describing the force caused by the potential difference is given by the following expression.

$$F_{dl} = \frac{\pi \varepsilon_o r U^2}{z}\ dyn \tag{6}$$

A simplified equation for the double layer force is given by equation 7. This equation assumes a separation distance, z, of 4 Å and uses a value of $8.85 \times 10^{-12}$ Coulombs per volt for the permittivity of free space, $\varepsilon_o$.

$$F_{dl} = 4dU^2\ \ mdyn \tag{7}$$

Assuming a maximum potential of 0.5 V and converting milliDynes to Newtons, the double layer force is approximately equal to

$$F_{dl} = 10^{-8}d\ \ \ N \tag{8}$$

with the particle diameter, d, having units of microns.

The second electrostatic force that influences particle adhesion is the image force. Ref. 6 describes the image force as arising from bulk excess charges on the particle and surface that cause a coulombic attraction. This force is described by Equation 9 where D is the dielectric constant for the separating material and is assumed to be 1 ($D_{air}$ = 1.0006 at 1 atm, $D_{vac}$ = 1), and $l$ is the distance between charge centers.

$$F_{imag} = \frac{q^2}{4\pi \varepsilon_0 D l^2} \tag{9}$$

Ref. 6 simplifies the image force equation by applying the following relation for the charge, q, where r is the particle radius, C is the capacitance and U is the potential difference.

$$q = CU = 4\pi \varepsilon_o r U \tag{10}$$

An estimation of the image force is then given by Equation 11 with d having units of microns. The equation assumes a charge density of 10 electrons per square micron which Ref. 6 claims is a reasonable charge density with the maximum possible being approximately 100 electronic charges per square micron.

$$F_{imag} = 3 \times 10^{-10} d^2\ \ \ N \tag{11}$$

### 2.1.3 Summary of Adhesion Forces

As described in the preceding sections, the dominant forces which act to adhere a particle to a surface are the Van der Waals, image and double layer forces. The Van der Waals force is expected to be the dominant force of these for particles with radii less than ~50μm. For larger particles, the electrostatic image force will match and exceed the Van der Waals force in magnitude. Figure 2.1 shows the adhesion forces as a function of particle radius. Equation 5 has been used to calculate the Van der Waals force using a Lifshitz-Van der Waals constant of 2.5 eV (~100 zJ).

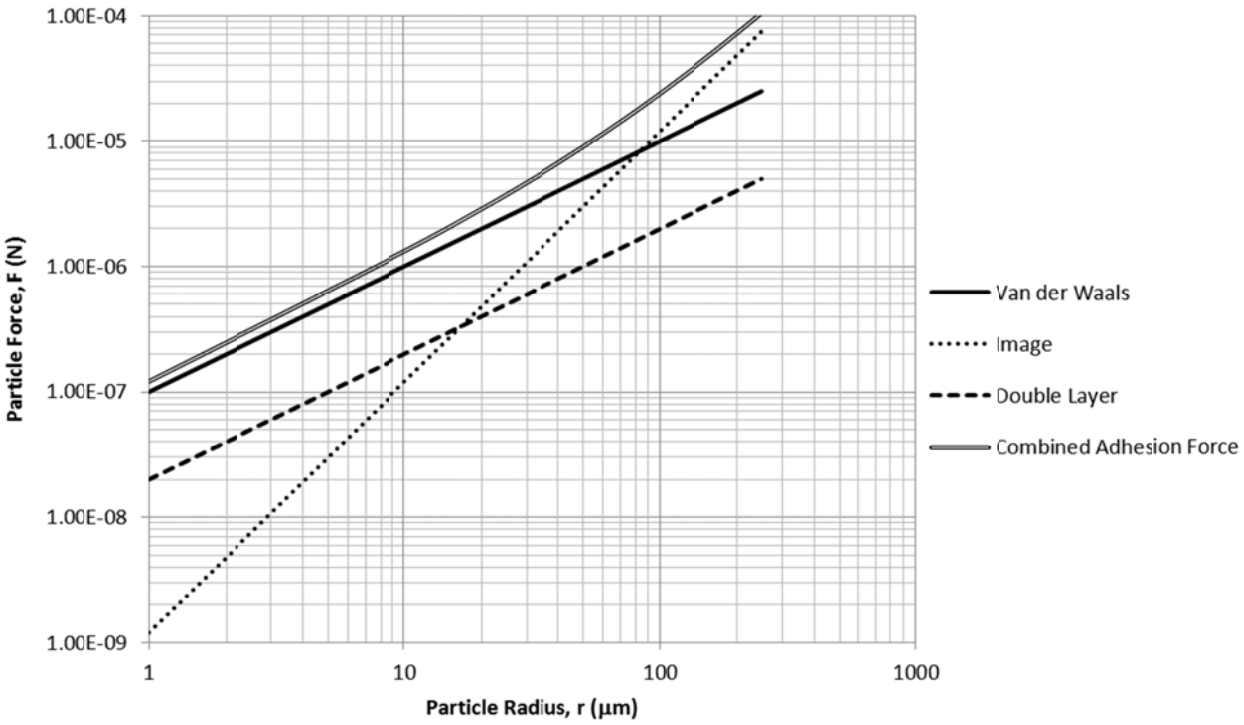


**Figure 2.1: Particle Adhesion Force**

For both types of adhesion forces, the theoretical equations which describe them rely on the assumption that a single perfectly spherical particle is interacting with a perfectly flat surface. This is rarely the case in nature where particles are likely to have rough, craggy surfaces and even the most carefully polished lens will have surface asperities. These variances in surface

geometry will reduce the magnitude of the adhesive force by increasing the separation distance between the particle and surface. An example of a real particle is shown in Figure 2.2 which shows a lunar dust particle. A particle found on earth would be more rounded due to weathering but would still exhibit a random, non-spherical geometry.

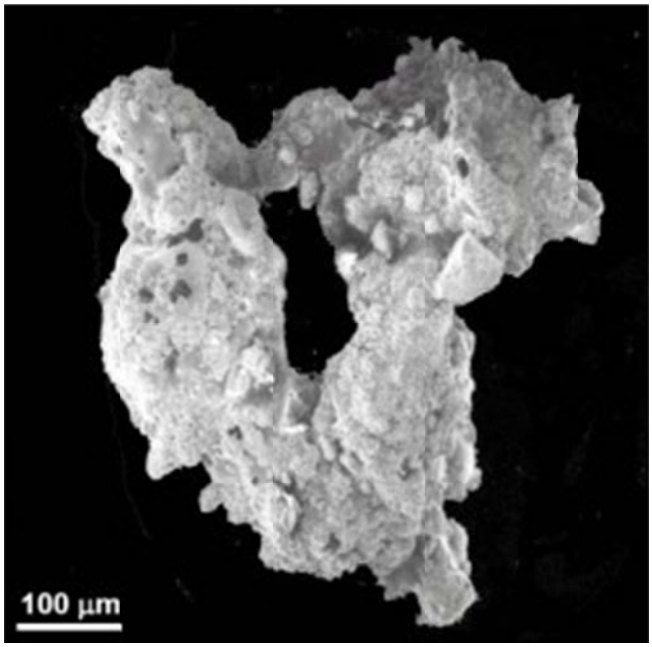


**Figure 2.2: Lunar Dust Particle**[22]

## 2.2 Removal Forces

Newton's second law of motion states that the time rate of change of a body's momentum is equal to the sum of the forces acting upon it. For the case of a particle resting on a surface, the adhesive forces and the particles resistance to deformation balance each other resulting in a stationary particle. To remove the particle from the surface, a force must be applied that is greater than the adhesive forces. In the absence of mechanical intervention, i.e. physically wiping off the particle, the only options are to apply an inertial force through vibrations or to push the particle off of the surface through drag forces. The following sections will describe the proposed removal forces in more detail.

### 2.2.1 Inertial forces

Perhaps the simplest method for removing an undesirable particle from a surface is to shake it off. If the surface could be caused to accelerate with a sufficient magnitude normal to its plane, the particle should be dislodged through its own momentum. The adhesive forces developed in the previous section are the forces which must be overcome to remove the particle[6]. With this in mind, the acceleration which is needed for removal can be calculated.

$$F_{adh} = m_{pt} a_{surf} = \frac{4}{3}\pi r^3 \rho a \tag{12}$$

The adhesive forces are repeated below for convenience where the Hamaker version of the Van der Waals equation has been chosen, and d=2r has been used in the double layer and image force estimations. The equations given below require r to have units of meters.

$$F_{adh} = F_{vdw} + F_{imag} + F_{dl} = \frac{Ar}{6z^2} + 1200r^2 + 2 \times 10^{-2} r \quad N \tag{13}$$

The individual accelerations required for each force are then given as follows.

$$a_{vdw} = \frac{A}{8\pi\rho z^2}\frac{1}{r^2} \ \ m/s^2 \tag{14}$$

$$a_{imag} = \frac{900}{\rho\pi}\frac{1}{r} \ \ m/s^2 \tag{15}$$

$$a_{dl} = \frac{3\times10^{-2}}{2\rho\pi}\frac{1}{r^2} \ \ m/s^2 \tag{16}$$

Figure 2.3 shows the expected acceleration required to remove glass microspheres from a surface based upon equations 14 through 16.

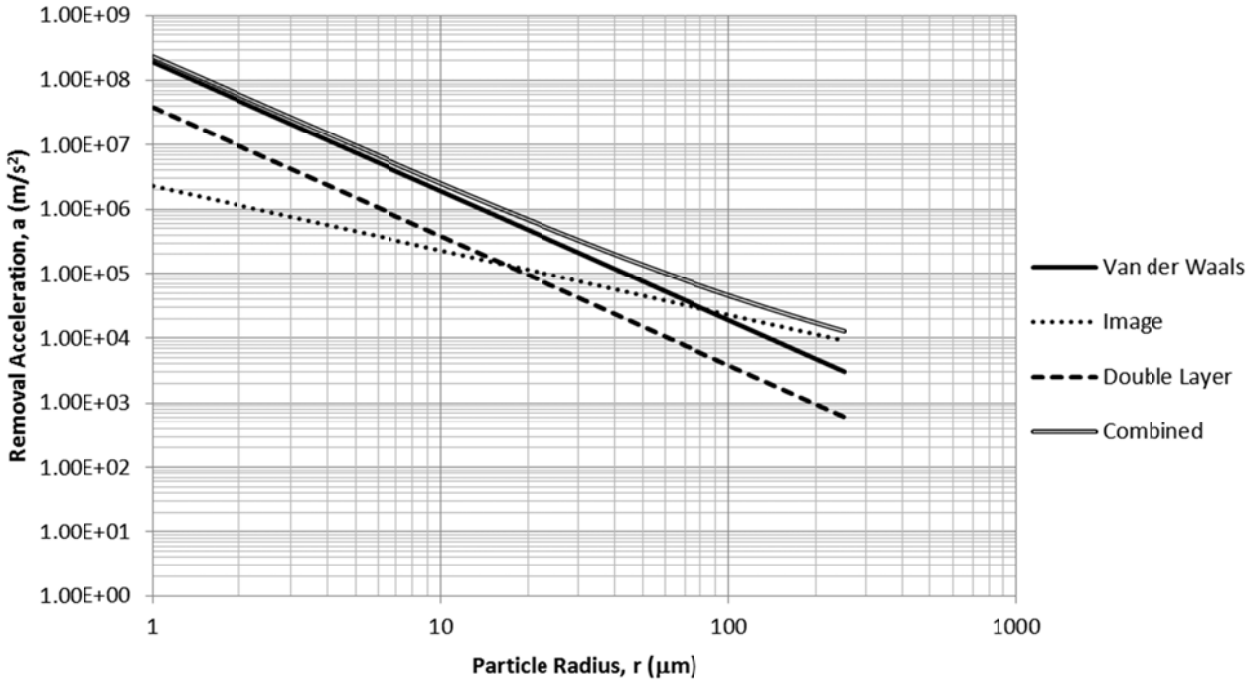


**Figure 2.3: Removal Acceleration for Glass Microspheres ($\rho$ = 125 kg/m$^3$)**

## 2.2.2 Particle Aerodynamic Forces

The concept of using a drag force on a particle to remove it from a surface is different from the inertial force in that the particle would be moved parallel to the surfaces plane. This method would use a pressurized gas blown across the surface to push the particle from the region of a lens that is visible through the camera. For some applications, such as on a planetary rover or satellite, a supply of gas would be limited and so this method would only be desirable as a last resort.

To remove a particle adhered to a surface using a drag force, the drag force must be greater than the static friction force between the particle and the surface[8].

$$F_D \geq F_f = \mu_{sf} F_{adh} \tag{17}$$

Ref. 5 states that the drag force on a particle on a surface is a function of the Reynolds number, given by $Re = \frac{\rho d u}{\mu}$, and can be approximated by Equation 18 for $Re \ll O(1)$ and by Equation 19 for $Re \gg O(1)$.

$$F_D \sim \mu R u \quad Re \ll O(1) \tag{18}$$

$$F_D \sim \rho (Ru)^2 \quad Re \gg O(1) \tag{19}$$

Equation 18 is a linear relation which scales with the radius of the particle for a given gas velocity, u, and dynamic viscosity, μ. The magnitude of the drag predicted by Eq. 19 quickly grows larger than that predicted by Eq. 18 because it is a function of the radius and velocity squared. For the particles and experimental setup described in Chapter 3, the Reynolds number ranges from ~0.5 to 50 for particles with diameters of 1 to 200 μm. This range does not clearly fit into that specified for Equation 18 or 19. However, only an order of magnitude estimation is required because the drag force on a particle will not be able to be measured. It is reasonable to assume that the force on a particle will be between the values predicted by the equations, with a conservatively low estimation being closer to Equation 18.

An additional aerodynamic force which can be considered in this application is a lift force. This force would act normal to the surface on a particle in opposition to the adhesive forces. Ref. 5 gives an approximation for this force, Eq. 20, derived from Bernoulli's equation. The lift force however is reduced significantly by the presence of the planar surface.

$$F_L \sim \rho (Ru)^2 \tag{20}$$

The aerodynamic forces are not meant to remove particles by themselves, but in combination with the inertial forces described in the previous section. It is proposed, that for particles which are too small to be removed by surface accelerations, the reduced adhesion force due to the inertial force will allow for the drag forces to push the particles from their position on the surface. Additionally, a potential problem with removing particles through vibrations is that if the particles are not ejected from the surface with sufficient energy to escape the electrostatic

forces they could be drawn back to the surface. By blowing air across the surface while inciting the surface accelerations, a small separation between the particle and surface could allow for a lift force as described by Eq. 20 to be generated and remove the particle from the surface. Equations 18 through 20 can be rewritten in terms of the Reynolds number to be given by Equations 21 through 23.

$$F_D \sim \frac{\mu^2}{2\rho} Re \quad Re \ll O(1) \tag{21}$$

$$F_D \sim \frac{\mu^2}{4\rho} Re^2 \quad Re \gg O(1) \tag{22}$$

$$F_L \sim \frac{\mu^2}{4\rho} Re^2 \tag{23}$$

Using this form of the equations, Figure 2.4 can be generated to estimate the aerodynamic forces. For an air velocity of 3.5 m/s and a particle diameter of 1 μm, the Reynolds number is 0.24 which gives a lift force of approximately $4 \times 10^{-12}$ N. The lift force scales with the square of the particle diameter so that for a particle with a 100 μm diameter, the lift force would be approximately $4 \times 10^{-8}$ N at a Reynolds number of 24. A comparison of the lift force with respect to the adhesion forces is shown in Figure 2.5. The airspeed used to calculate the lift force curve is 3.5 m/s which results in a lift force three orders of magnitude smaller than the combined adhesion force for a 20 micron diameter particle. This means that an airspeed of approximately 110 m/s would be required to overcome the adhesion force.

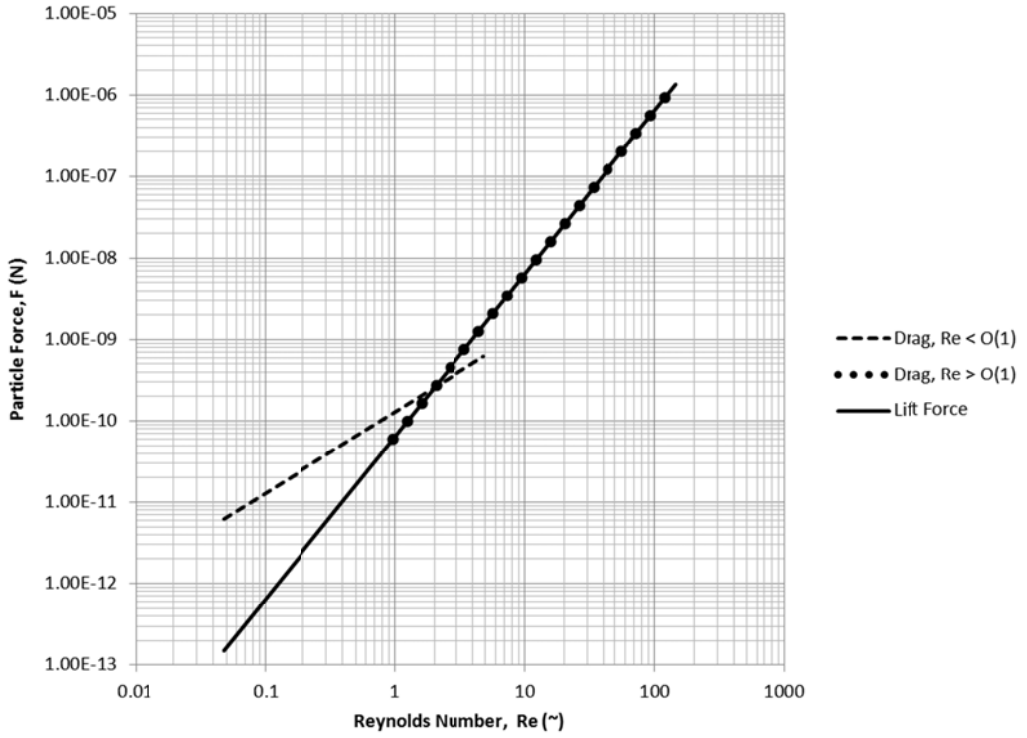


**Figure 2.4: Particle Aerodynamic Force (air at standard atmosphere)**

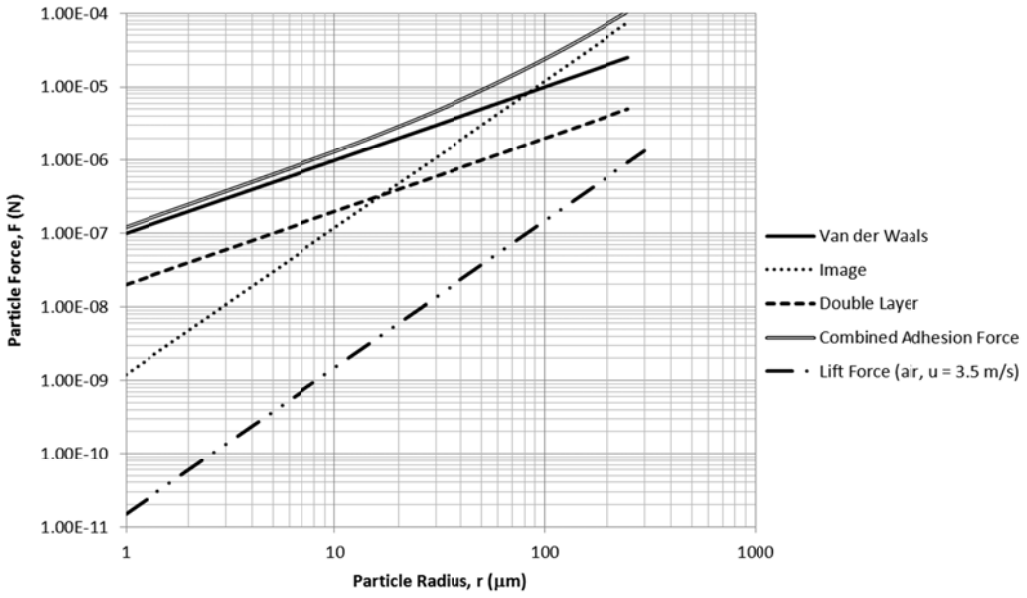


**Figure 2.5: Particle Force Comparison**

## 2.3 Surface Acceleration

To develop accelerations sufficient to dislodge particles on the surface of a lens, the lens can be excited at one of its natural frequencies. A non-magnifying lens or filter can be thought of as a flat plate with uniform thickness. The differential equation which describes the response of such a rectangular plate is given by Eq. 24[20, 21]. The displacement of the plate normal to its plane is given by the function *w* which is a function of two spatial coordinates and time.

$$-D_E\left(\frac{\partial^4 w(x,y,t)}{\partial x^4}+\frac{\partial^4 w(x,y,t)}{\partial x^2 \partial y^2}+\frac{\partial^4 w(x,y,t)}{\partial y^4}\right)=\rho w_{tt}(x,y,t) \tag{24}$$

The constant, $D_E=\frac{Eh^3}{12(1-\nu^2)}$, is known as the plate flexural rigidity with E the elastic modulus of the plate and h the thickness.

Assuming that the solution for the plate equation is separable, i.e. $w(x,y,t)=X(x)Y(y)T(t)$, it can be re written as follows,

$$-D_E(X''''Y+2X''Y''+Y'''')T=\rho\ddot{T}XY \tag{25}$$

$$\frac{-\rho}{D_E}\frac{\ddot{T}}{T}=\frac{X''''}{X}+\frac{2X''Y''}{XY}+\frac{Y''''}{Y} \tag{26}$$

A solution to the spatial portion of this equation is

$$\begin{aligned} X(x)Y(y) &= A_1\sin\alpha x\sin\gamma y+A_2\sin\alpha x\cos\gamma y+A_3\cos\alpha x\sin\gamma y \\ &+A_4\cos\alpha x\cos\gamma y+A_5\sinh\alpha_1 x\sinh\gamma_1 y \\ &+A_6\sinh\alpha_1 x\cosh\gamma_1 y+A_7\cosh\alpha_1 x\sinh\gamma_1 y \\ &+A_8\cosh\alpha_1 x\cosh\gamma_1 y\,, \end{aligned} \tag{27}$$

$$\alpha^2+\gamma^2=\alpha_1^2+\gamma_1^2=\beta^2=\left(\frac{\omega^2\rho}{D_E}\right)^2 \tag{28}$$

This solution however is not very useful for the purposes of this research. It can only be solved in terms of one of the coefficients and so cannot give any information about the magnitude of the vibrations. The temporal solution on the other hand gives a valuable insight into the response of a plate. The temporal solution of the plate will have the form,

$$T(t) = \text{asin}\,\omega t + b\cos\omega t \tag{29}$$

where $\omega$ is the frequency at which the plate is vibrating. The spatial solution is only dependent on the spatial variables, which means the velocity and acceleration of the plate can be calculated by differentiating the temporal solution with respect to time.

$$u(x, y, t) = X(x)Y(y)\dot{T}(t) \tag{30}$$

$$a(x, y, t) = X(x)Y(y)\ddot{T}(t) \tag{31}$$

The significance of this lies in the observation that the magnitude of the acceleration at a point on the plate is proportional to that of the deflections by a factor of $\omega^2$ or the velocity by a factor of $\omega$. This means that by inciting a very small deflection in the lens at a high frequency a sufficient force to dislodge a particle could be developed.

The response of a vibrating plate is often largest when it is vibrating at one of its natural frequencies. To determine the natural frequencies of the experimental device used for this research, the plate equation could be solved. The boundary conditions of the slide, however, are not well suited to this equation so instead a finite element program was used to determine the natural frequencies and mode shapes of the slide. The mode shapes are desired so that a frequency could be chosen to drive the slide which would cause the largest portion of the slide to be active. The next section will further explain this.

### 2.3.1 Natural Frequency Estimation

To estimate the natural frequencies of the glass slide used for this research, a model of the slide was constructed in Patran and analyzed using NASTRAN. 3D quad elements were used, and the boundary conditions applied to the ends are zero displacement and zero rotation. Only the portion of the slide that was bonded to the piezoelectric stacks as shown in Figure 3.3 had these conditions applied.

The thickness dimension of the slide, 0.00099 m, was interpreted as 0 by Patran. The solution of this problem was to scale the dimensions and stiffness of the slide by a factor S based on a method known as Froude Scaling[22]. The dimensions and properties of the glass slide and their scaled values are shown in Table 2.2. Glass properties for 96% silica glass from Ref. 26 were used.

**Table 2.2: Froude Scaled Glass Slide Properties[23]**

| | Actual Value | Scale Factor | Scaled Value |
|---|---|---|---|
| Length | 0.076 m | S | 76 m |
| Width | 0.025 m | S | 25 m |
| Thickness | 0.00099 m | S | 0.99 m |
| Density * | 2180 kg/m$^3$ | 1 | 2180 kg/m$^3$ |
| Elastic Modulus * | 68 GPa | S | 68 GPa |
| Poisson's Ratio * | 0.19 ~ | 1 | 0.19 ~ |

*Properties for 96% Silica Glass

After analyzing the model, the predicted frequencies were scaled by $1/S^{1/2}$ according to Ref. 21. The predicted frequencies and scaled frequencies are listed in Table 2.3 and the first five predicted mode shapes are shown in Figure 2.6 through Figure 2.10.

**Table 2.3: Predicted Frequencies**

| | PATRAN Output | Scaled |
|---|---|---|
| mode | Freq | Freq |
| | Hz | Hz |
| 1 | 38 | 1215 |
| 2 | 70 | 2225 |
| 3 | 104 | 3299 |
| 4 | 149 | 4719 |
| 5 | 198 | 6256 |
| 6 | 239 | 7561 |
| 7 | 289 | 9139 |
| 8 | 301 | 9525 |
| 9 | 330 | 10450 |
| 10 | 370 | 11689 |
| 11 | 415 | 13126 |
| 12 | 499 | 15767 |
| 13 | 615 | 19433 |

It was previously mentioned that a mode shape with the most active area was desired for removing particles. This is evidenced in the following images of the mode shapes of the slide. The first mode shows the largest deflection at the center of the slide, while the third mode shows a node line at the center. Along a node line, the slides surface does not experience any deflections and so no particles would be dislodged. The number of node lines on the slide increases with increasing frequency which means that a larger portion of the slide would be ineffective for removing particles. To get around this limitation though, the slide could be cycled through its natural frequencies to ensure that all portions of the slide are activated at some point in time.

At the beginning of this research, the mode shapes of the slide were experimentally visualized by placing a layer of salt across the surface. When the slide was driven at its natural frequencies the salt would settle along the node lines. Figure 2.11 shows the mode shape of the slide at a frequency of 2018 Hz. It closely resembles the predicted mode shape at 6256 Hz. The boundary conditions of the slide used for the salt image were significantly different than those used for modeling so the difference in frequencies is not unexpected.

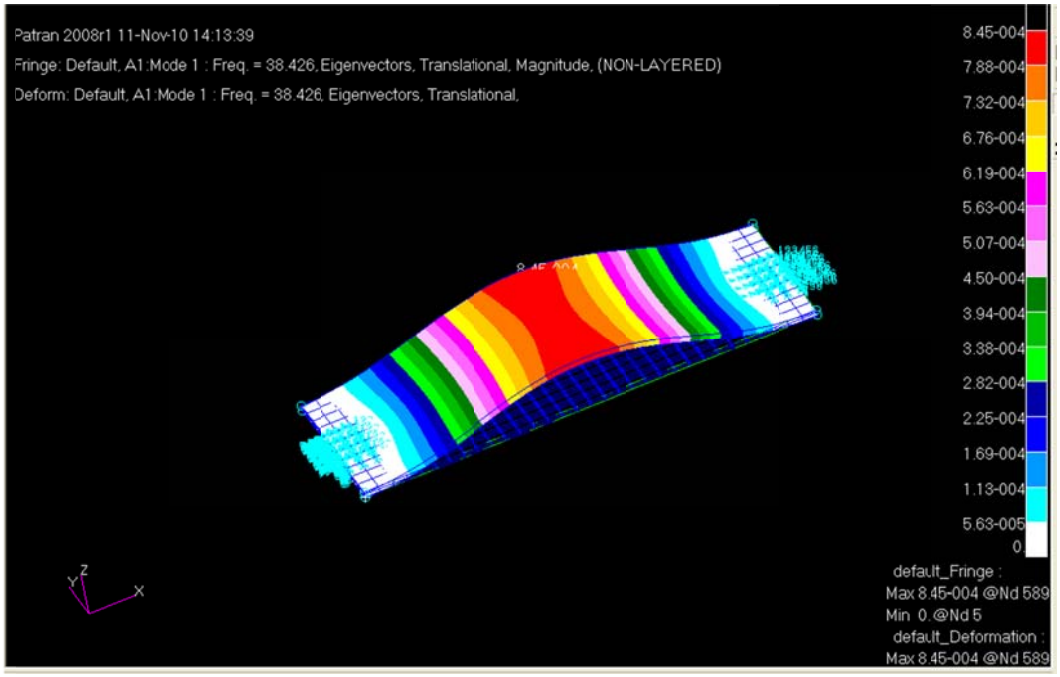


**Figure 2.6: Mode 1, f = 1215 Hz**

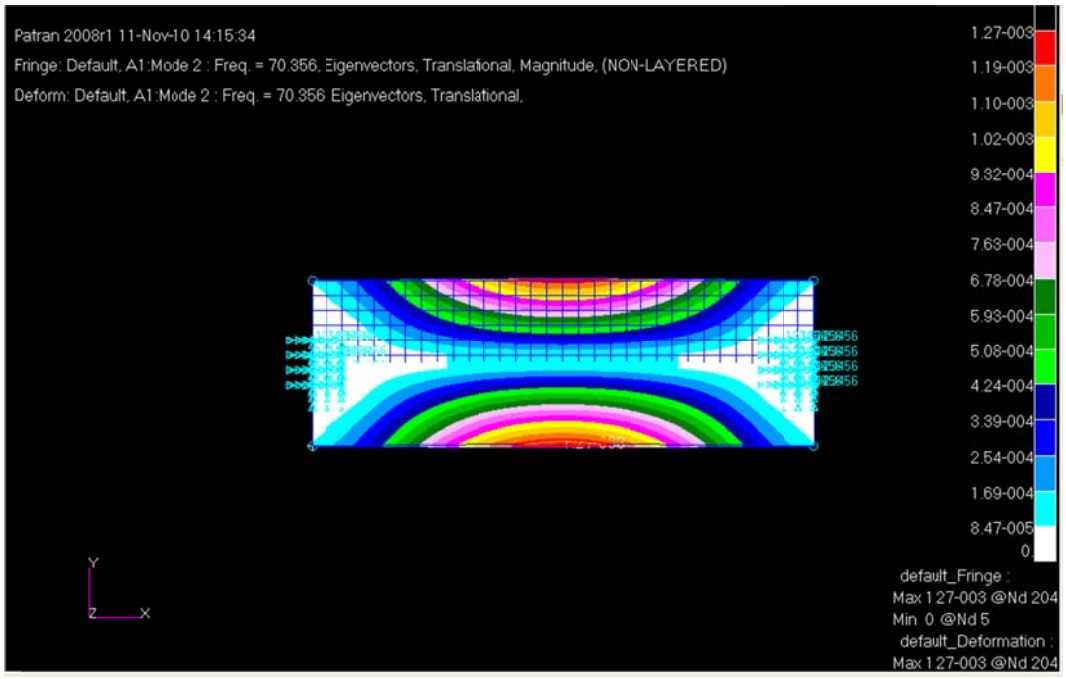


**Figure 2.7: Mode 2, f = 2225 Hz**

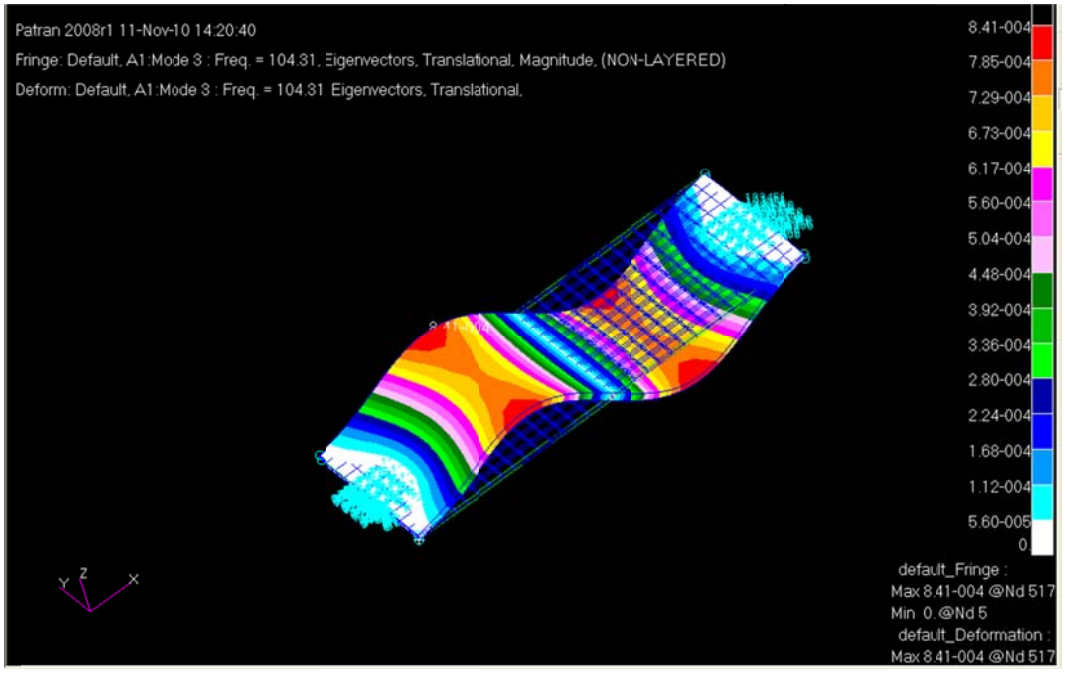


**Figure 2.8: Mode 3, f = 3299 Hz**

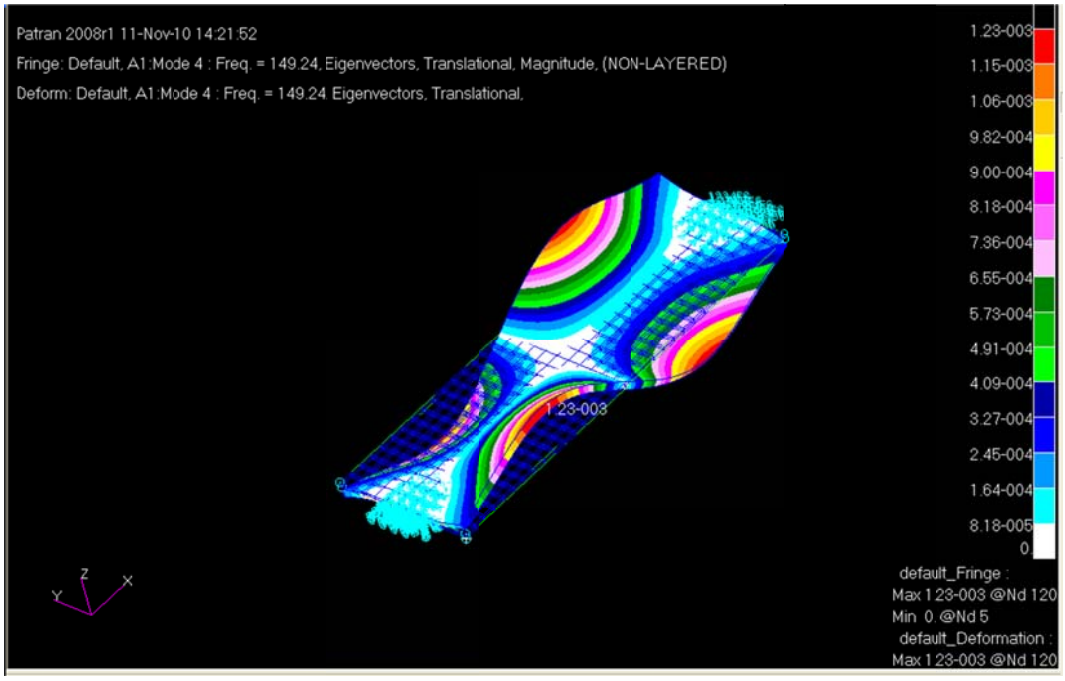


**Figure 2.9: Mode 4, f = 4719 Hz**

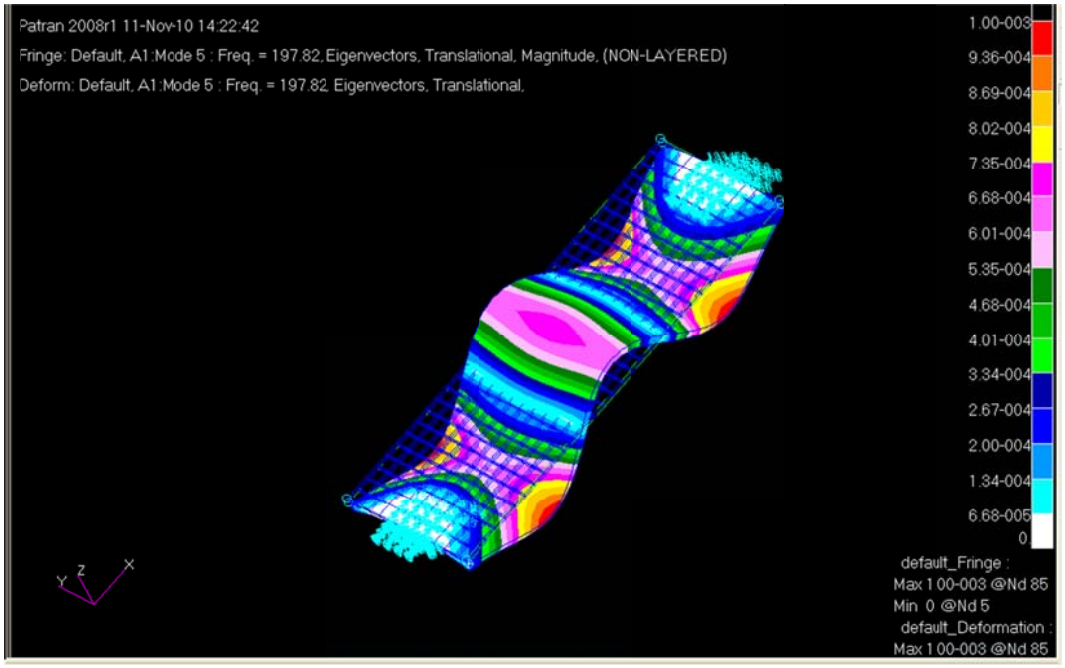


**Figure 2.10: Mode 5, f = 6256 Hz**

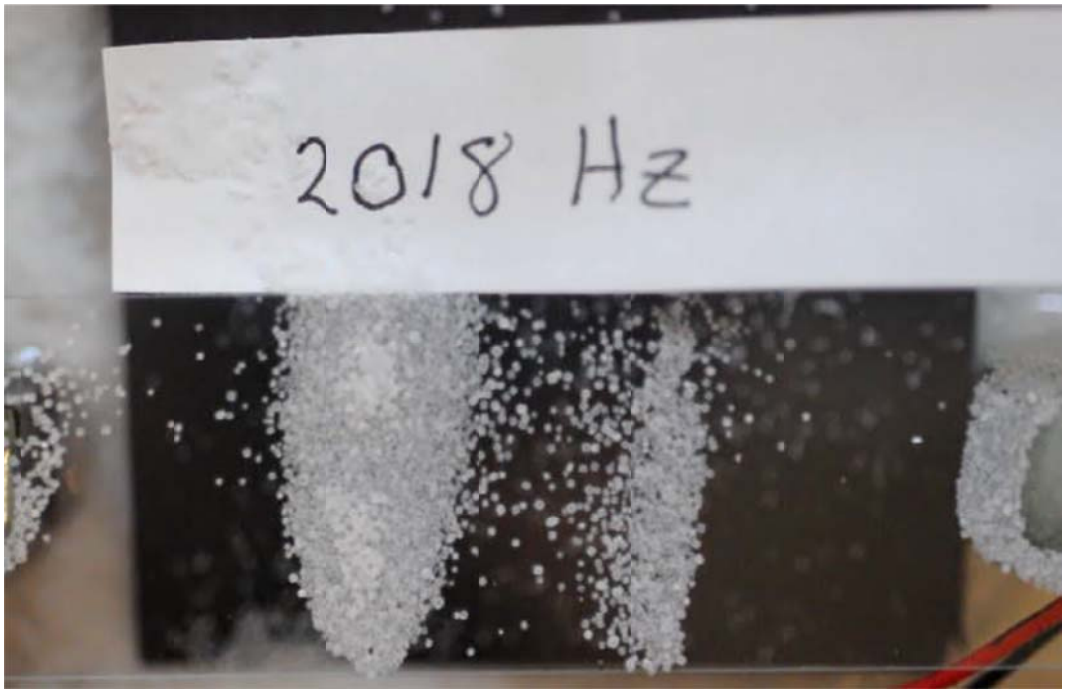


**Figure 2.11: Salt Mode Shape, f = 2018 Hz**

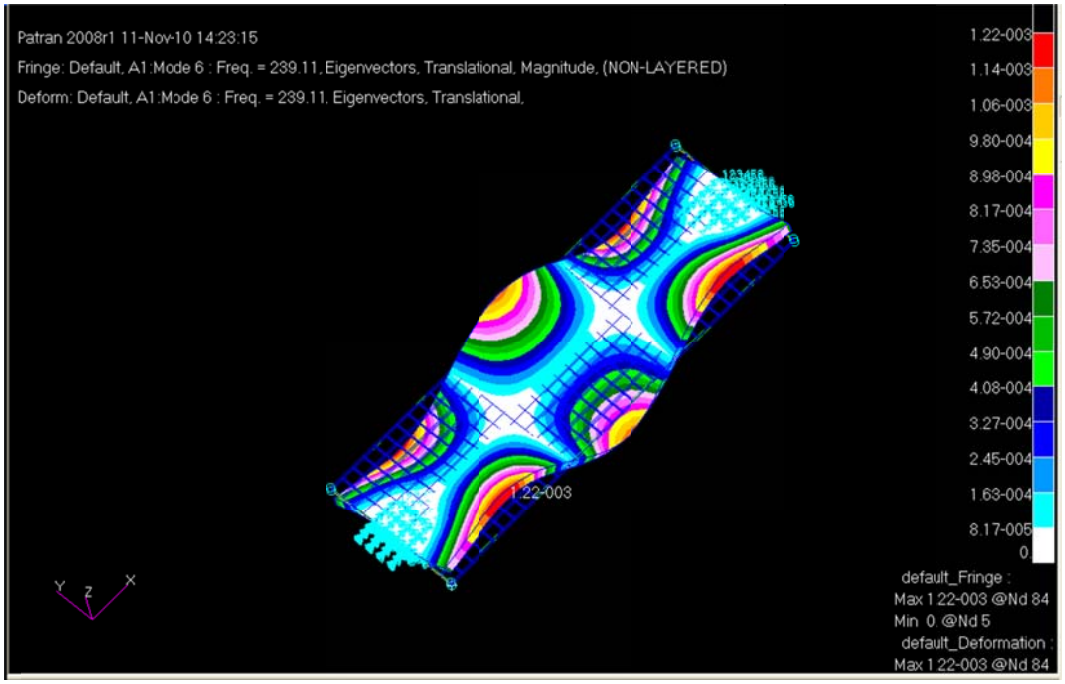


**Figure 2.12: Mode 6, f = 7561 Hz**

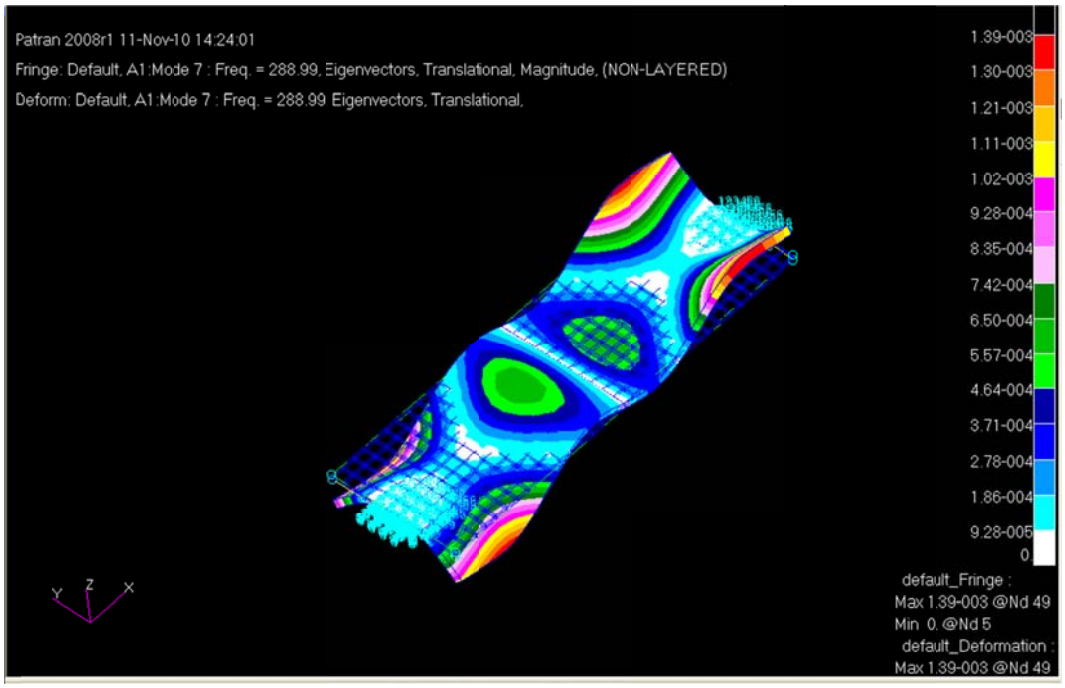


**Figure 2.13: Mode 6, f = 9139 Hz**

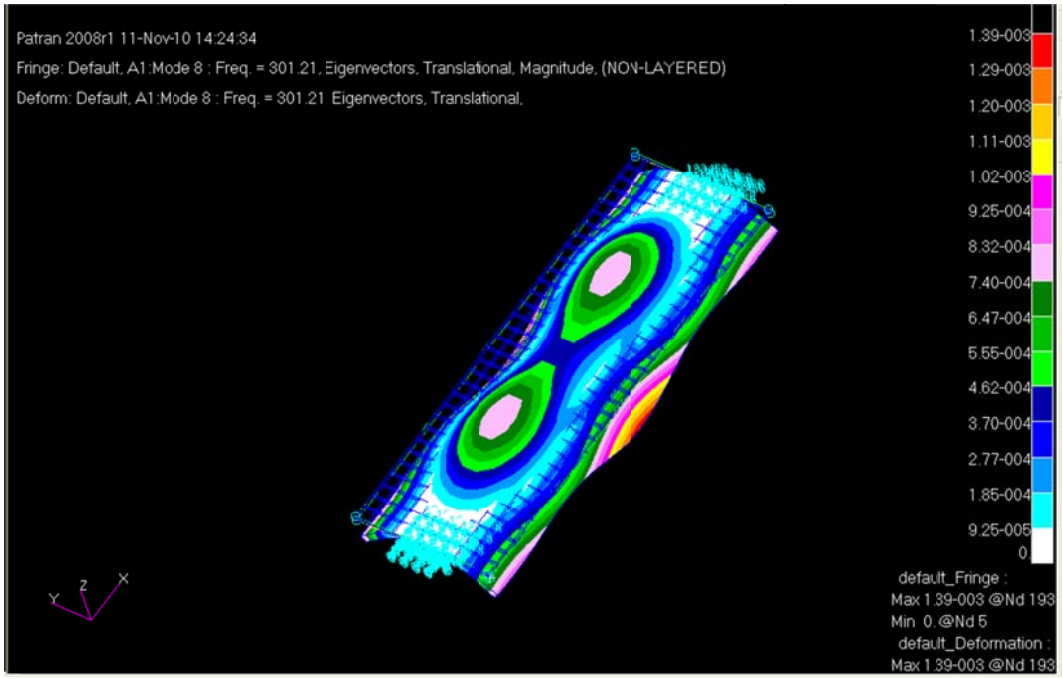


**Figure 2.14: Mode 8, f = 9525 Hz**

# 3. Experimental Setup and Procedures

The experimental work for this research was performed in the Adaptive Aerostructures Laboratory at the University of Kansas, Lawrence campus. The following sections will detail the experimental equipment used as well as the procedures carried out during testing.

## 3.1 Experimental Device

Camera lenses and filters are typically circular in shape and often have bonded support structures. To simplify the experimental device for this research a rectangular microscope slide was used instead. The goal of this research is not determining the varied response of glass plates due to geometry, but simply the potential for achieving high enough acceleration on the plate to remove particles. For this reason, the use of the microscope slide is justified.

The microscope slide used is of standard size with a 3" length and 1" width. The thickness of the slide is approximately 0.04". This slide was attached to two piezoelectric stack actuators which were themselves attached to a seismic base as shown in Figure 3.1. When a periodic voltage is applied to the stack actuators, they expand and contract causing a vertical displacement of the slide attachment points. This movement is shown exaggerated in Figure 3.2 with the slide first mode of vibration.

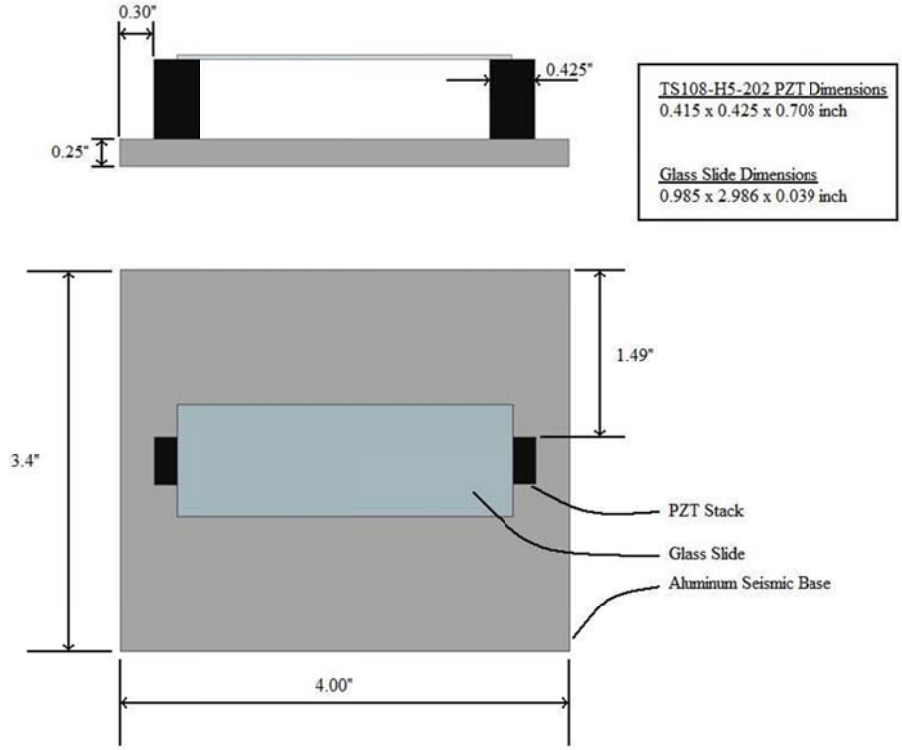


**Figure 3.1: Shaker Assembly Dimensions**

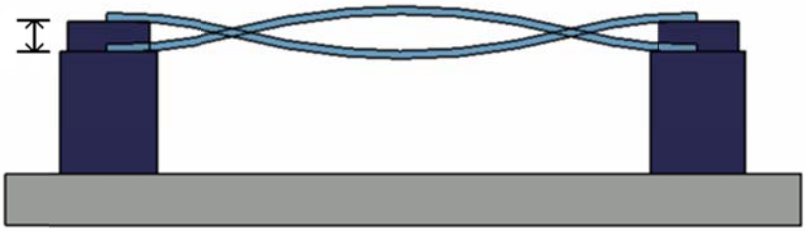

**Figure 3.2: Stack Actuator Movement (not to scale)**

The stacks used are TS18-H5-202 piezoelectric stack actuators available from piezo.com. The technical sheet for these actuators can be obtained from Ref. 24, and the relevant specifications are shown in Table 3.1. To attach the actuators to the base plate as shown in Figure 3.3, a two part epoxy was used. This epoxy was also used to attach the slide to the actuators.

**Table 3.1: Stack Actuator Specifications[24]**

| TS18-H5-202 Specifications | |
|---|---|
| Dimensions (mm) | 10 x 10 x 18 |
| Compressive Strength | $8.8 \times 10^8$ **N/m$^2$** |
| Mass (grams) | 16 |
| Capacitance (nF) | 6500 |
| Stiffness | $2.3 \times 10^8$ **N/m** |
| Response Time (μs) | 50 |
| Rated Voltage (+Vp) | 100 |
| Free Deflection (μm) | 14.5 |
| Blocked Force (N) | 3,388 |
| Operating Temperature ($^o$C) | -20 to +80 |

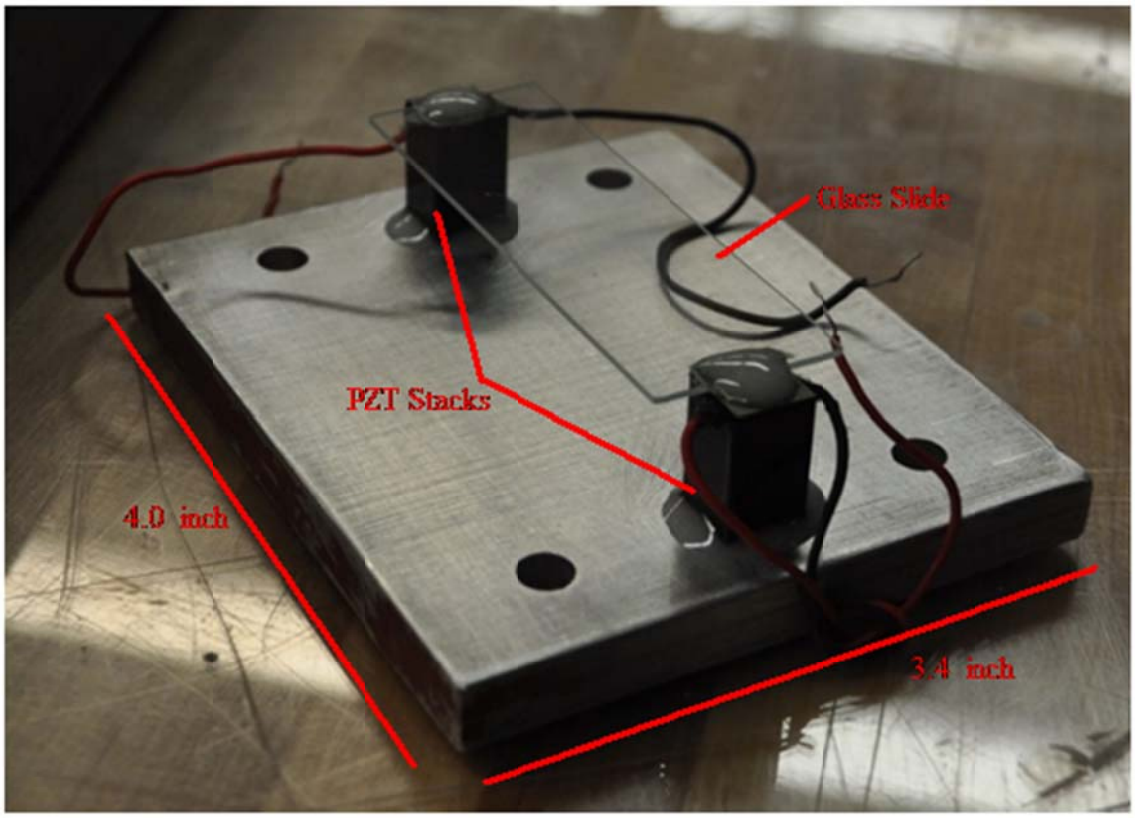


**Figure 3.3: Shaker Assembly**

During testing, the slide shaker assembly needed to be held in a vertical orientation. To achieve this, the aluminum base was bolted to a wooden frame. The shaker assembly and the frame are shown Figure 3.4.

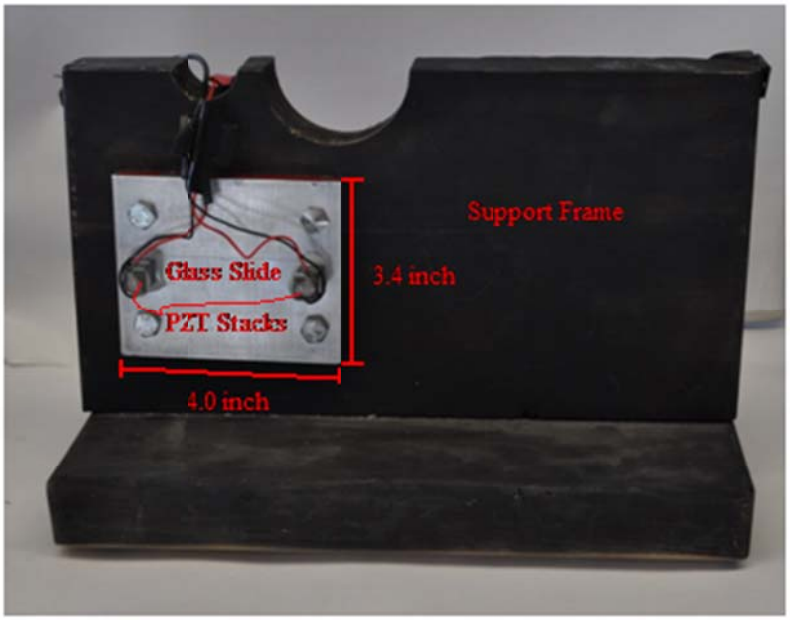


**Figure 3.4: Shaker Assembly mounted on Frame**

## 3.2 Lab Equipment

To drive the piezoelectric stacks a signal generator is required along with some means of amplification. The signal generator used was a GW Instek SFG-2004 Function Generator. This function generator has a maximum output of 4 MHz using a sine, square or triangle wave.

During initial testing, a Piezo Systems inc. Linear Amplifier, Model EPA-104, was used to amplify the signal from the function generator. However due to the capacitance of the piezoelectric stacks, the power output of this amplifier was not sufficient to achieve the goals of the research. Figure 3.5 shows the measured power delivered by the Piezo Systems amp to a single stack and a two stack configuration in series as a function of driving frequency. As can be seen, the power output of the amplifier drops drastically with increasing frequency. The curve shown for the two stack configuration is the total power delivered to both stacks. The values for

this curve are approximately double that for the single stack curve which means that regardless of the configuration, the amplifier can only deliver a certain amount of power to a single stack. To verify that the amplifier was properly set up, the measured voltage can be plotted vs. frequency (Figure 3.6) and compared with the published[25] performance for the EPA-104 amplifier (Figure 3.7). The capacitive load for a single stack is 6.5 μf and 3.25 μf for two stacks in series.

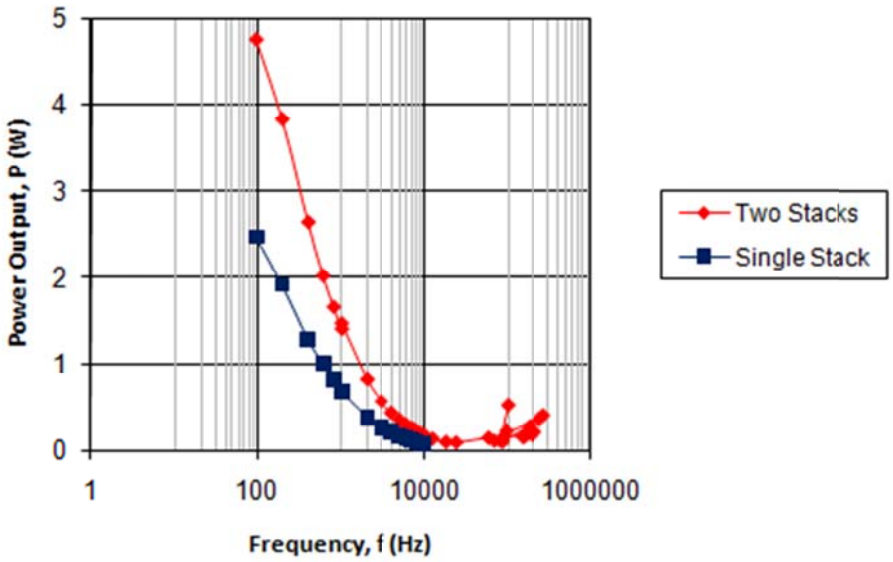


**Figure 3.5: Linear Amplifier Power Output**

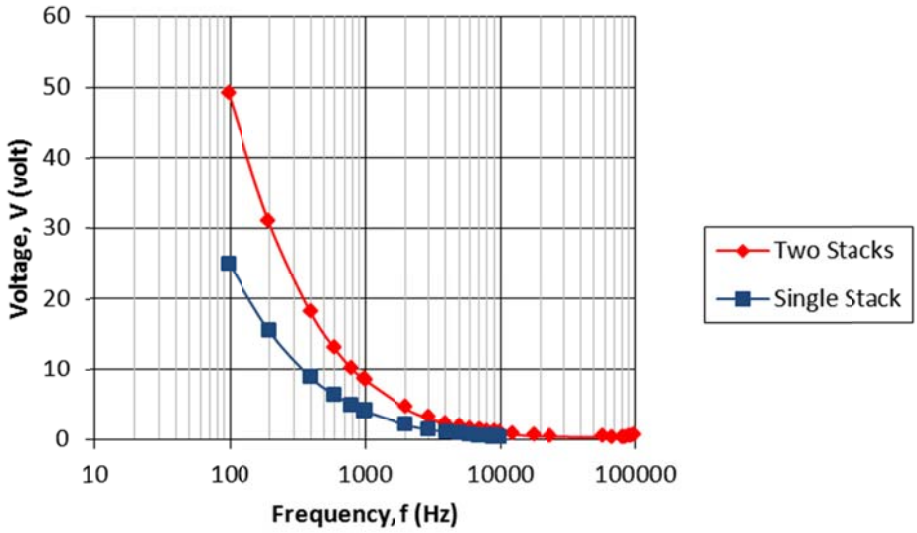


**Figure 3.6: Linear Amplifier Voltage Output**

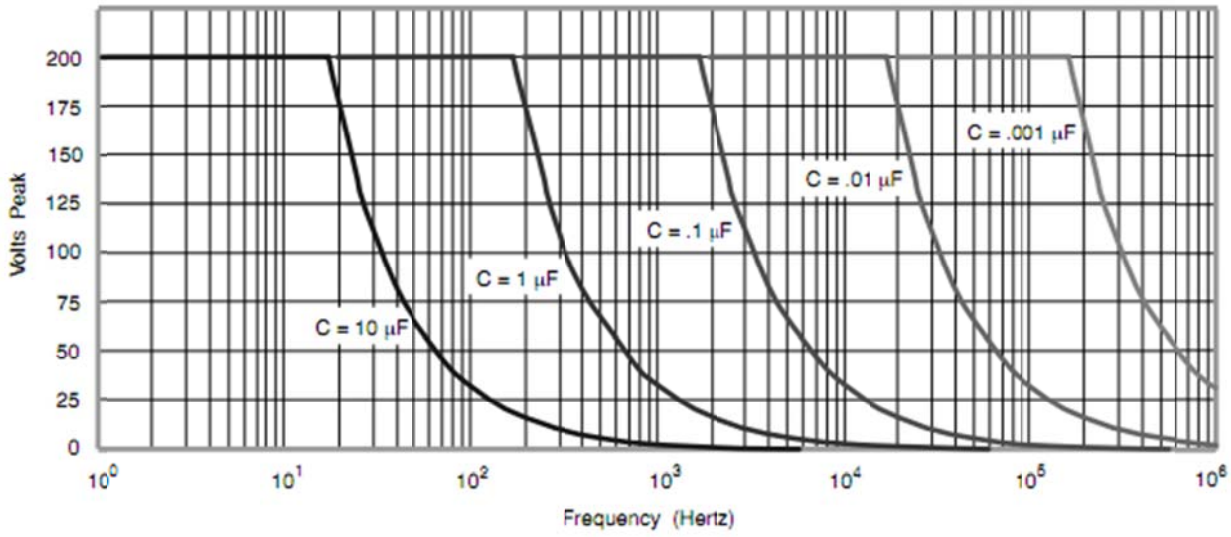


**Figure 3.7: EPA-104 Published Voltage Output**[25]

Due to the drop in power output at increasing frequencies, the glass was not sufficiently energized to remove particles. To solve this problem a circuit[26] was constructed using a MOSFET which could amplify the signal from the function generator using a direct current power supply. A schematic for this circuit is shown below. The DC power supply used for this set up is a GW Instek GPS-18500.

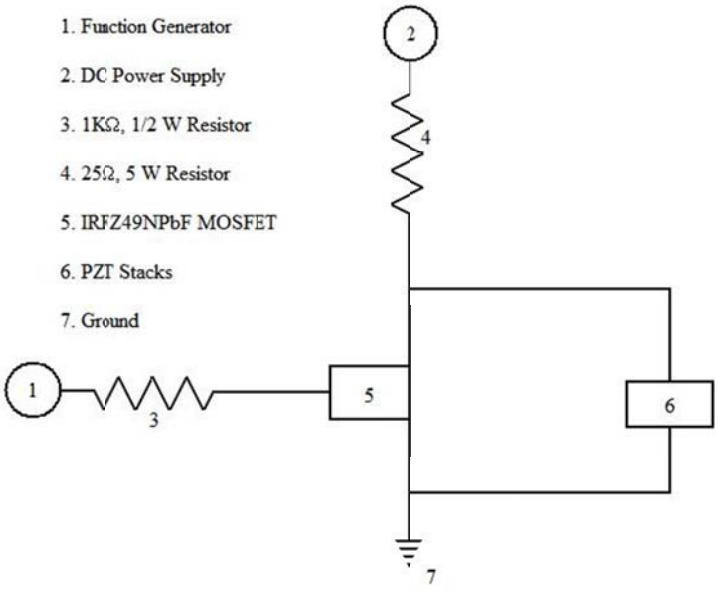


**Figure 3.8: MOSFET Amplifier Circuit Diagram[26]**

Using this circuit, significantly more power was delivered to the piezoelectric stacks. This is illustrated in the following figures. Figure 3.9 shows a comparison of the power supplied to the stacks by the Piezo systems amp and the MOSFET amp. Figure 3.10 shows the voltage applied across the stacks which are in series.

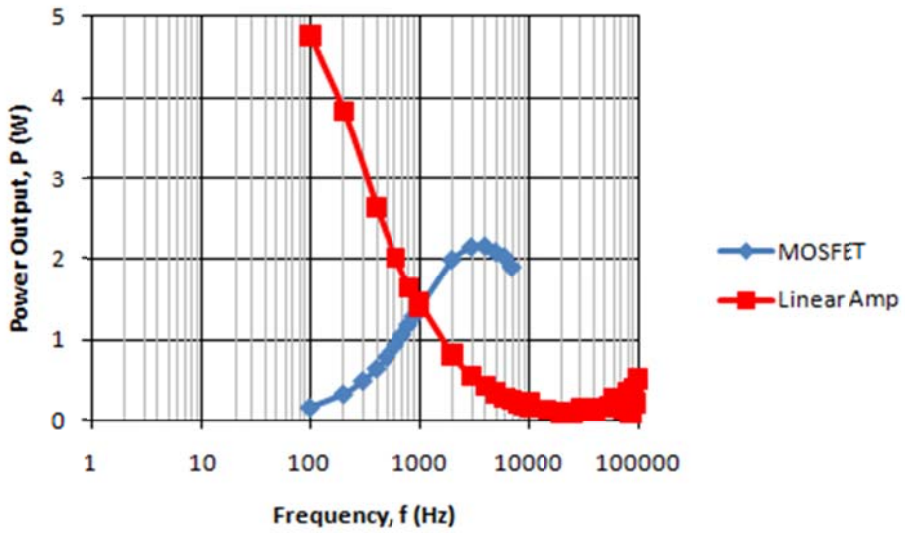


**Figure 3.9: Power Comparison for Linear and MOSFET Amp**

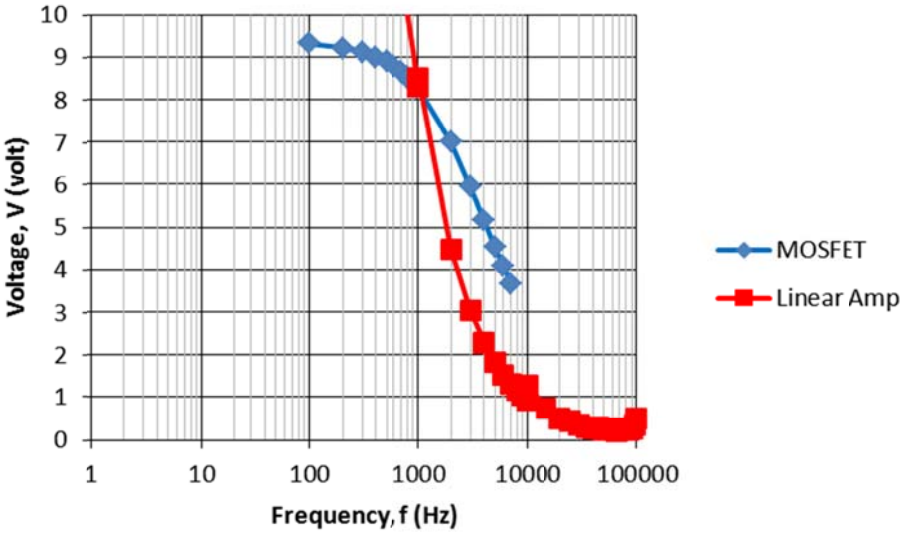


**Figure 3.10: Voltage Comparison for Linear and MOSFET Amp**

Measurement of the voltage across the stacks was achieved using a Fluke 8845A 6 ½ Digit Precision Multimeter. The multimeter was also used to verify the driving frequency at the stacks. The following table contains the data used to generate the preceding plots. In the case of the MOSFET amp, voltage readings above 7 kHz were not able to be measured because the multimeter would interfere with the circuit. The MOSFET circuit, while effective in providing

higher voltages to the stacks, was sensitive to static charges and electrical interference. It was however functional at higher frequencies even though the voltages could not be measured. The results presented in the following chapter used frequencies that could be measured.

**Table 3.2: Amplifier Voltage Data**

| Linear Amplifier | | | | MOSFET Amplifier | |
|---|---|---|---|---|---|
| One Stack | | Double Stack | | Double Stack | |
| Measured f (Hz) | Voltage (V) | Measured f (Hz) | Voltage (V) | Measured f (Hz) | Voltage (V) |
| 97.7 | 24.90 | 97 | 49.00 | 97.68 | 9.33 |
| 197.6 | 15.40 | 196.5 | 30.90 | 195.6 | 9.22 |
| 397.3 | 8.90 | 398.4 | 18.02 | 297.3 | 9.12 |
| 599.1 | 6.37 | 599.2 | 12.85 | 396.9 | 9.01 |
| 796.7 | 4.99 | 795.6 | 10.09 | 497.6 | 8.89 |
| 992.4 | 4.11 | 992.7 | 8.31 | 597.7 | 8.78 |
| 1995 | 2.15 | 1992 | 4.49 | 696.5 | 8.66 |
| 2994 | 1.46 | 2978 | 3.04 | 799.3 | 8.54 |
| 4004 | 1.15 | 3983 | 2.29 | 900.3 | 8.40 |
| 5000 | 0.91 | 5004 | 1.84 | 999.7 | 8.27 |
| 6008 | 0.75 | 6004 | 1.54 | 2003 | 7.00 |
| 7006 | 0.64 | 6959 | 1.33 | 2995 | 5.94 |
| 7986 | 0.55 | 7968 | 1.16 | 3991 | 5.16 |
| 8975 | 0.48 | 8969 | 1.03 | 5001 | 4.53 |
| 9945 | 0.43 | 9965 | 0.93 | 6022 | 4.07 |
| | | 12400 | 0.73 | 7007 | 3.66 |
| | | 17900 | 0.51 | | |
| | | 23600 | 0.43 | | |
| | | 57500 | 0.35 | | |
| | | 67400 | 0.28 | | |
| | | 80000 | 0.26 | | |

The last major piece of equipment used for this research was a Polytec model OFV 056 Scanning Laser Vibrometer, shown in Figure 3.11. The laser vibrometer was used to determine the natural frequencies of the glass slide assembly, as well as the surface accelerations. The laser vibrometer was operated from a control station next to the vibrometer.

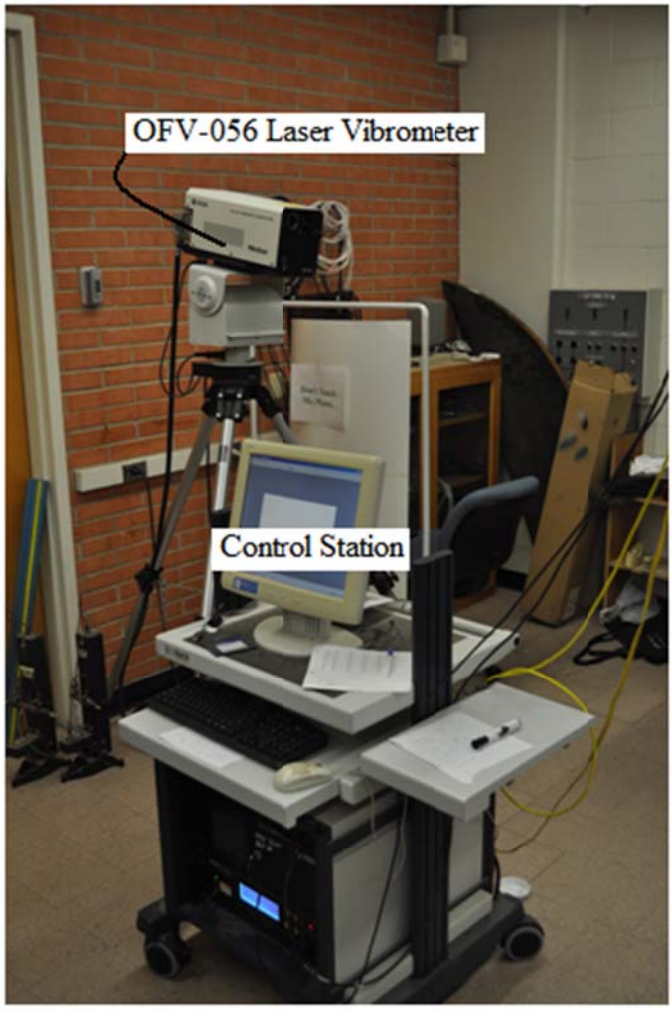


**Figure 3.11: Polytec OFV 056 Laser Vibrometer**

During testing, the shaker assembly and the amplifier setup were placed in front of the laser vibrometer as shown in Figure 3.12. Initially, the slide was left clear, but the laser vibrometer had difficulty scanning the surface. To correct this, the slide was blacked out using a permanent marker as shown in Figure 3.13.

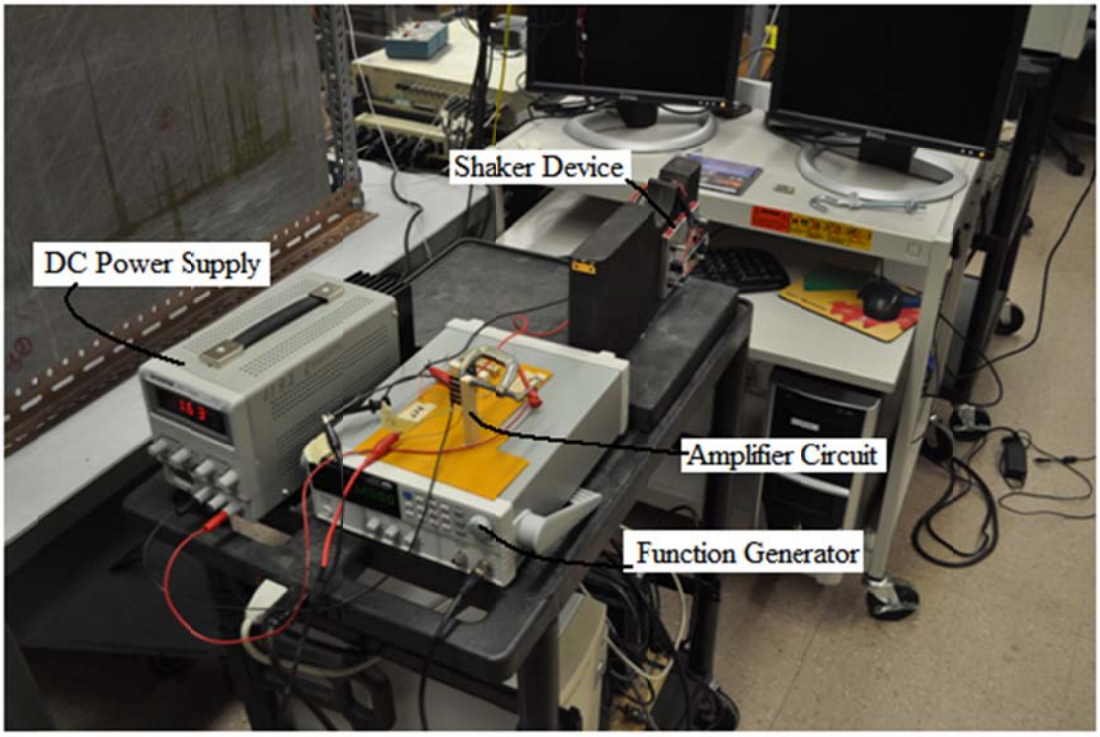


**Figure 3.12: Laser Vibrometer Equipment Setup**

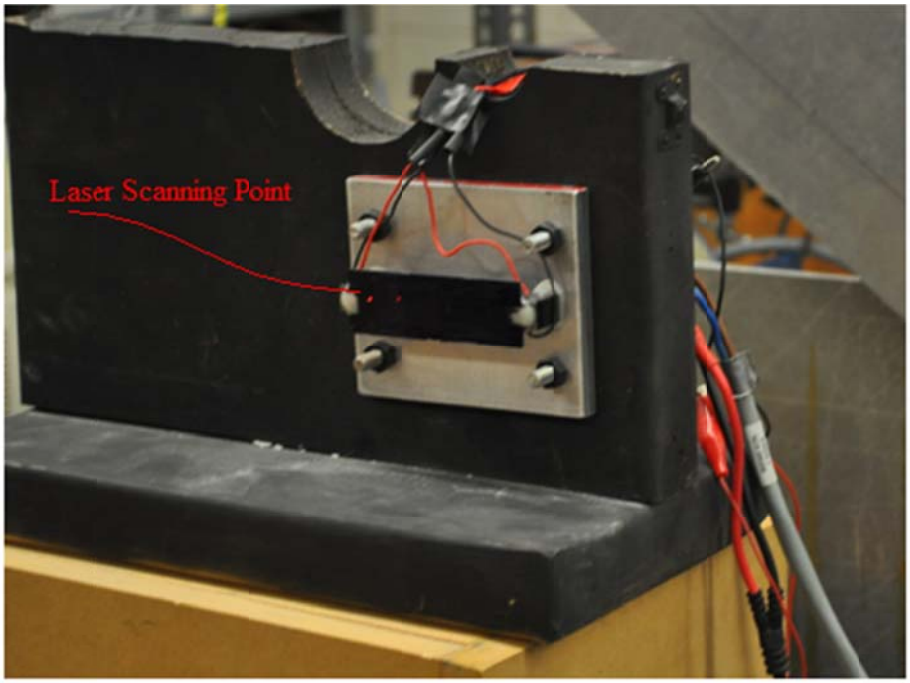


**Figure 3.13: Laser Vibrometer Scanning Point**

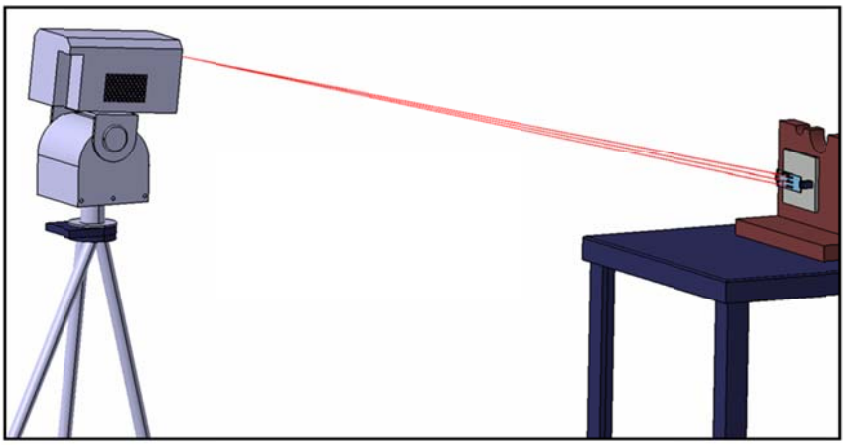

**Figure 3.14: Disposition of Laser Vibrometer and Shaker Device**

Additional equipment used for this research includes a Nikon D5000 digital single lens reflex (SLR) camera with a 60mm AF Micro Nikkor lens. A microscope was also used for high magnification images.

## 3.3 Glass Microspheres

A number of different types of particles were considered for the purpose of representing environmental debris including dust which had collected on surfaces around the lab, sand and dirt, and glass microspheres. The glass microspheres were chosen because they closely resemble the ideal smooth and spherical particle that the adhesive force equations assume. Initial testing was conducted with un-calibrated glass microspheres. The bulk density of these particles is unknown, though an estimation of the particle diameter was achieved. The diameter of these particles ranged from ~15μm to 150 μm. This estimation was found by comparing the particles to a wire with known diameter under a microscope.

The results of the experiments conducted with the un-calibrated glass microspheres were promising so further experiments were conducted using 3M K1 Glass Microspheres which have a similar particle diameter to that used in the initial experiments. The properties of these particles are shown below.

**Table 3.3: 3M K1 Glass Microsphere Properties[27]**

| 3M K1 Glass Microspheres | |
|---|---|
| Crush Strength | 250 psi |
| Density | 0.125 g/cc |
| Particle Diameter | 30 - 115 μm |


**Figure 3.15: 3M K1 Glass Microspheres**

## 3.4 Wind Tunnel Setup

To provide a consistent airflow across the glass slide, a small wind tunnel was constructed. This tunnel consisted of a 2 inch diameter PVC pipe, a small DC motor and a DC power supply. The motor, power supply and tunnel inlet are shown in Figure 3.16. The main goal of this assembly was to provide a smooth flow of air over the slide with a consistent velocity. The velocity of the airflow was determined using an Extech model 407123 Hot Wire Anemometer shown in Figure 3.17.

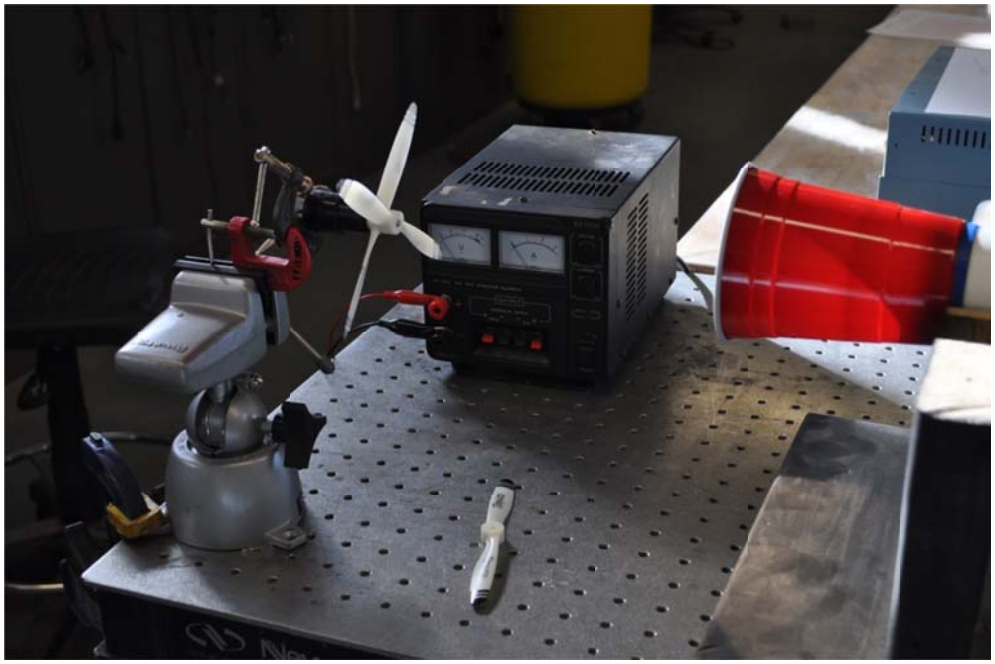

**Figure 3.16: DC Motor and Power Supply**


**Figure 3.17: Extech 407123 Hot Wire Anemometer**

The outlet of the tunnel was placed so that the center of the airflow would impinge upon the glass slide as shown in Figure 3.18.

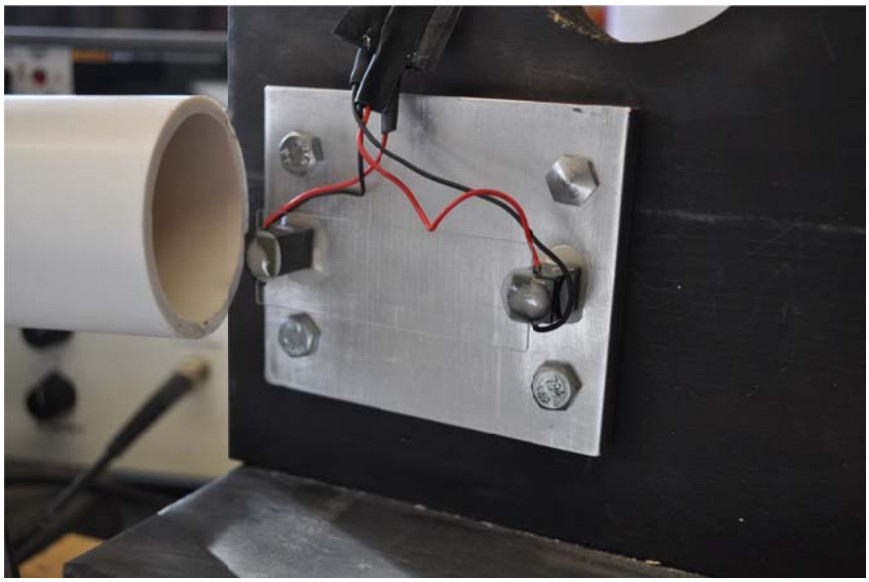

**Figure 3.18: Wind Tunnel Outlet**

## 3.5 Testing Procedure

The experiments for which results are reported in the following Chapter proceeded as follows.

A layer of glass microspheres was deposited on the glass slide while it was in a horizontal position. The slide assembly was then rotated so that the slides plane was vertical. To hold the slide vertical, the entire assembly was fixed to a wood frame using bolts.

After placing the wood frame at the exit of the wind tunnel, the electrical leads to the piezoelectric stacks were connected to the MOSFET circuit. The power supply was then switched on and the supply was increased to its maximum. The function generator was then turned on, with the output gain set to the minimum. After selecting a frequency of operation on

the function generator, the gain was increased until the glass microspheres on the slide were seen to fall away from the surface. The wind tunnel was then switched on.

When no more particles were observed leaving the slide, the function generators gain was turned down, then the wind tunnel was switched off.

### 3.5.1 Image Capture

To capture the images shown in the following chapter, the test procedure was modified as follows.

Before applying the glass microspheres, a 0.003 inch diameter wire was fixed across the surface of the slide to provide a size reference. After applying the glass and allowing the excess to fall away, the assembly was placed under a microscope. The Nikon Camera was positioned so that a photograph could be taken through the microscope. The wire was affixed to the piezoelectric stacks using tape and was removed during testing.

The slide was then mounted to the wood frame and the glass slide was excited with the function generator. The wind tunnel was not used so that the particles which remained after the cleaning could be photographed under the microscope. Once this was done, the slide was re attached to the wood frame and the wind tunnel was used without the function generator to remove the glass microspheres. Another image of the slide was taken, and then the final test was conducted using the wind tunnel and the function generator with one last image being taken after the tests completion.

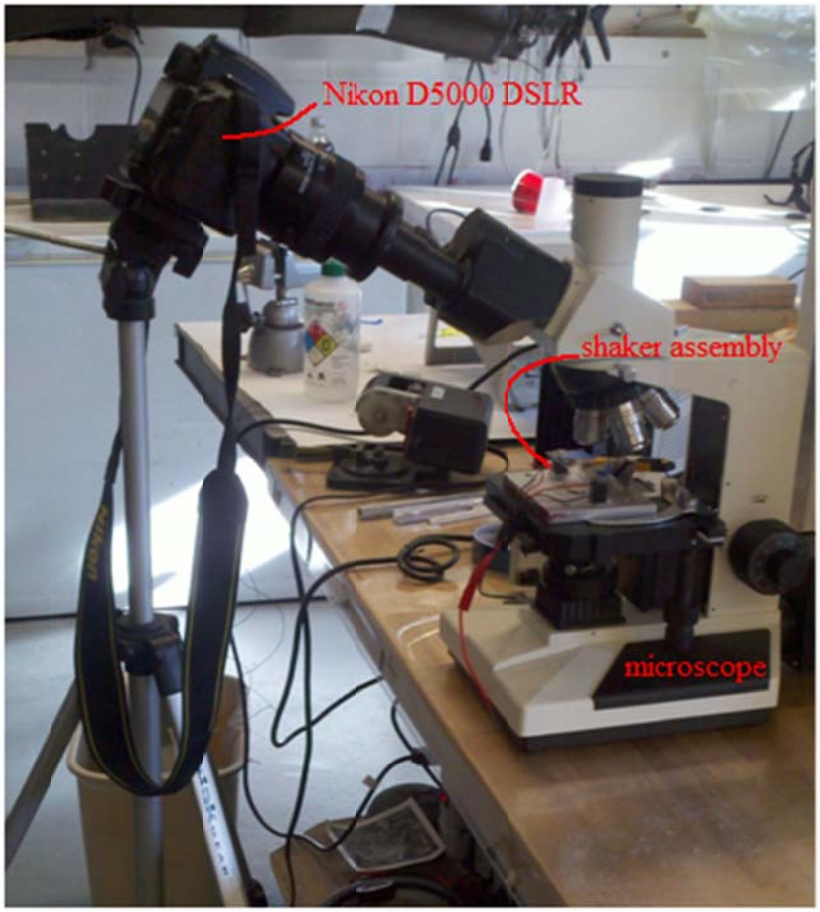


**Figure 3.19: Microscope and Camera Positioning**

# 4. Results

The following sections will present the results of the experimental research beginning with the FEM model validation using the Polytech laser vibrometer. A macroscopic illustration of particles fouling an image as well as the removal of the particles will be presented. Following this, a visual argument for this thesis will be presented using microscopic images of a dynamically cleaned slide.

## 4.1 Laser Vibrometer Testing

As was mentioned in Chapter 2, the solution to the plate equation does not give the magnitude of the response for a vibrating plate. This is true of the finite element analysis performed as well. To determine the magnitude of accelerations on the glass slide, the laser vibrometer described in Chapter 3 was used.

The laser vibrometer is meant to be used as a modal analysis tool for structures. It works by scanning the surface of a structure which is being driven by a random signal and determining the velocity of the response of the surface. From this, the natural frequencies and modal response of the structure can be determined. For this application, the laser vibrometer was used primarily to determine the velocity of the response at a single frequency. However, a simple modal analysis of the slide was performed to validate the finite element model. The natural frequencies determined from this test are shown in the following table along with the frequencies predicted by the finite element analysis. The results show that the finite element analysis is acceptably close and the difference in the frequencies can be attributed to the actual boundary conditions on the device.

**Table 4.1: Experimentally Determined Natural Frequencies**

| Mode No. | Predicted | Laser Vibrometer |
|---|---|---|
| 1 | 1215 Hz | 1200 Hz |
| 2 | 2225 Hz | 2404 Hz |
| 3 | 3299 Hz | 3608 Hz |
| 4 | 4719 Hz | 3790 Hz |
| 5 | 6256 Hz | 5006 Hz |
| 6 | 7561 Hz | 6214 Hz |
| 7 | 9139 Hz | 7347 Hz |
| 8 | 9525 | 8600 Hz |

For determination of the surface velocity, a set of nine points, Figure 4.1, were scanned on the glass slide. The precise location of the points was not recorded due to difficulties in measuring the lasers image on the slide during testing, but the numbering and approximate position of the points are shown in Figure 4.2.

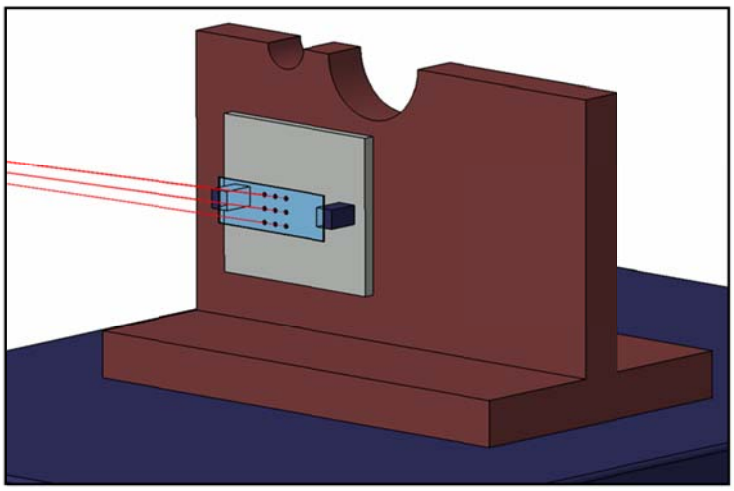

**Figure 4.1: Laser Vibrometer Scan Points (not to scale)**

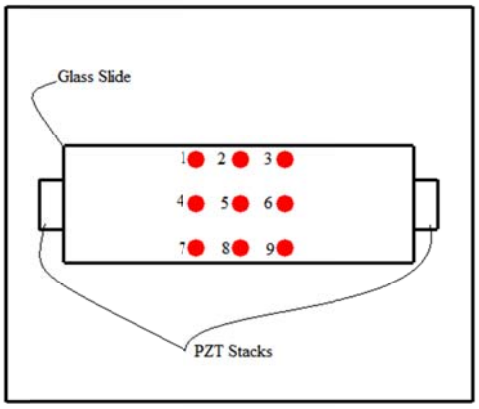


**Figure 4.2: Laser Vibrometer Scan Point Numbering**

For all of the tests using the laser vibrometer, the MOSFET amplifier described in Chapter 3 was used with a sinusoidal signal and a DC voltage of 18.95V. The laser vibrometer software reports root mean squared velocity which can be converted to the velocity amplitude by the relation,

$$u_{rms} = \frac{u_{max}}{\sqrt{2}}$$

The data collected for the nine individual points is presented in Table 4.2 followed by the calculated accelerations and displacements.

**Table 4.2: Laser Vibrometer Velocity Data**

RMS Surface Velocity (μm/sec)

| Mode No. | Frequency (Hz) | Point 1 | Point 2 | Point 3 | Point 4 | Point 5 | Point 6 | Point 7 | Point 8 | Point 9 | Average | Max |
|---|---|---|---|---|---|---|---|---|---|---|---|---|
| 1 | 1200 | 2031 | 2031 | 1937 | 1903 | 1899 | 1812 | 1763 | 1804 | 1725 | 1878 | 2031 |
| 2 | 2405 | 300 | 314 | 325 | 320 | 334 | 325 | 324 | 333 | 329 | 323 | 334 |
| 3 | 3608 | 1345 | 1286 | 1083 | 1440 | 1488 | 1282 | 1489 | 1501 | 1409 | 1369 | 1501 |
| 4 | 3790 | 301 | 276 | 251 | 553 | 319 | 290 | 889 | 551 | 305 | 415 | 889 |
| 5 | 5006 | 1206 | 963 | 746 | 1000 | 814 | 730 | 874 | 824 | 731 | 876 | 1206 |
| 6 | 6214 | 894 | 627 | 622 | 938 | 571 | 563 | 917 | 595 | 517 | 694 | 938 |
| 7 | 7347 | 518 | 503 | 514 | 1043 | 492 | 539 | 1858 | 1052 | 558 | 786 | 1858 |
| 8 | 8600 | 1763 | 1912 | 2093 | 1907 | 1830 | 2042 | 2145 | 1997 | 2014 | 1967 | 2145 |

**Table 4.3: Laser Vibrometer Calculated Acceleration Data**

RMS Surface Acceleration ($m/sec^2$)

| Mode No. | Frequency (Hz) | Point 1 | Point 2 | Point 3 | Point 4 | Point 5 | Point 6 | Point 7 | Point 8 | Point 9 | Average | Max |
|---|---|---|---|---|---|---|---|---|---|---|---|---|
| 1 | 1200 | 15 | 15 | 15 | 14 | 14 | 14 | 13 | 14 | 13 | 14 | 15 |
| 2 | 2405 | 5 | 5 | 5 | 5 | 5 | 5 | 5 | 5 | 5 | 5 | 5 |
| 3 | 3608 | 30 | 29 | 25 | 33 | 34 | 29 | 34 | 34 | 32 | 31 | 34 |
| 4 | 3790 | 7 | 7 | 6 | 13 | 8 | 7 | 21 | 13 | 7 | 10 | 21 |
| 5 | 5006 | 38 | 30 | 23 | 31 | 26 | 23 | 27 | 26 | 23 | 28 | 38 |
| 6 | 6214 | 35 | 24 | 24 | 37 | 22 | 22 | 36 | 23 | 20 | 27 | 37 |
| 7 | 7347 | 24 | 23 | 24 | 48 | 23 | 25 | 86 | 49 | 26 | 36 | 86 |
| 8 | 8600 | 95 | 103 | 113 | 103 | 99 | 110 | 116 | 108 | 109 | 106 | 116 |

**Table 4.4: Laser Vibrometer Calculated Deflection Data**

RMS Surface Deflection (mm)

| Mode No. | Frequency (Hz) | Point 1 | Point 2 | Point 3 | Point 4 | Point 5 | Point 6 | Point 7 | Point 8 | Point 9 | Average | Max |
|---|---|---|---|---|---|---|---|---|---|---|---|---|
| 1 | 1200 | 0.2694 | 0.2694 | 0.2569 | 0.2524 | 0.2519 | 0.2403 | 0.2338 | 0.2393 | 0.2288 | 0.2491 | 0.2694 |
| 2 | 2405 | 0.0199 | 0.0208 | 0.0215 | 0.0212 | 0.0221 | 0.0215 | 0.0214 | 0.0220 | 0.0218 | 0.0214 | 0.0221 |
| 3 | 3608 | 0.0593 | 0.0567 | 0.0478 | 0.0635 | 0.0656 | 0.0566 | 0.0657 | 0.0662 | 0.0622 | 0.0604 | 0.0662 |
| 4 | 3790 | 0.0126 | 0.0116 | 0.0105 | 0.0232 | 0.0134 | 0.0122 | 0.0373 | 0.0231 | 0.0128 | 0.0174 | 0.0373 |
| 5 | 5006 | 0.0383 | 0.0306 | 0.0237 | 0.0318 | 0.0259 | 0.0232 | 0.0278 | 0.0262 | 0.0232 | 0.0279 | 0.0383 |
| 6 | 6214 | 0.0229 | 0.0161 | 0.0159 | 0.0240 | 0.0146 | 0.0144 | 0.0235 | 0.0152 | 0.0132 | 0.0178 | 0.0240 |
| 7 | 7347 | 0.0112 | 0.0109 | 0.0111 | 0.0226 | 0.0106 | 0.0117 | 0.0402 | 0.0228 | 0.0121 | 0.0170 | 0.0402 |
| 8 | 8600 | 0.0326 | 0.0354 | 0.0387 | 0.0353 | 0.0339 | 0.0378 | 0.0397 | 0.0370 | 0.0373 | 0.0364 | 0.0397 |

## 4.2 Macroscopic Cleaning

The overall goal of this research is to determine if it is possible to remotely remove particles from a lens which are obscuring an image. The following images show that it is feasible to dynamically clean a lens in such a case.

Figure 4.3 shows the glass slide with a layer of the 3M glass microspheres distributed across it. The microspheres were deposited on the slide while it was parallel to the ground and then the slide was rotated to a vertical orientation. The slide was cleaned thoroughly prior to the application of the microspheres using methyl alcohol to remove any surface contaminants so that the particles remaining after the slide was rotated were held in place entirely by the forces described in Chapter 2. Figure 4.4 shows the slide after the actuators have been excited. The frequency used for this case was 1200 Hz using the maximum power output of the amplifier as shown in Figure 3.9.

**Figure 4.3: Distributed Glass Microspheres on Slide (scale 2:1)**

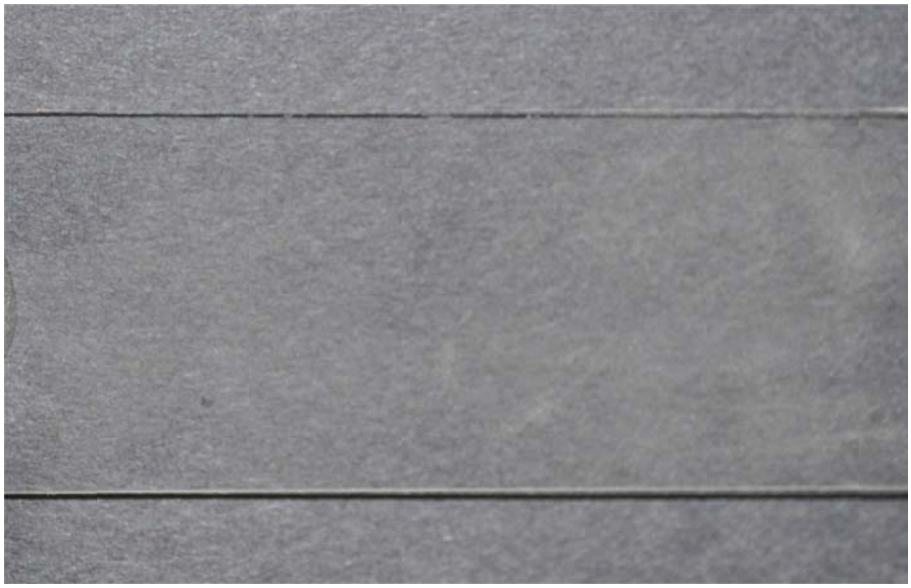

**Figure 4.4: Slide Post Cleaning, f = 1200 Hz (scale 2:1)**

The previous images show that the particles can be dynamically removed, but do little to convey the need for such cleaning. As an example of the need for cleaning, a standard US Nickel was fixed to the aluminum base of the shaker assembly and a picture of the Nickel was taken through the clean slide. Glass microspheres were then deposited on the slide in the same manner as that shown in Figure 4.3 and the slide was excited to remove the particles.

Figure 4.5 shows the nickel before the glass microspheres were placed on the glass slide. As can be seen, a good level of detail is visible in the image. Figure 4.6 shows the nickel as seen through the slide after the glass microspheres have been deposited. Some glass microspheres settled onto the nickel because it is open to the environment, but the particles on the slide are clearly obscuring the image of the nickel.

Following the dusting of the slide, the actuators were excited at a frequency of 1200 Hz. This frequency was selected primarily because this mode shape has the largest percentage of glass

actively deflecting. Figure 4.7 shows the nickel after the cleaning of the slide. The obscuring particles have been successfully removed and the details of the coin are visible once again.


**Figure 4.5: Nickel Prior to dusting**

**Figure 4.6: Nickel Obscured by Glass Microspheres**


**Figure 4.7: Nickel Post Cleaning, f =1200 Hz**

## 4.3 Microscopic Cleaning

The images presented in the previous section prove that particles which have agglomerated to an extent sufficient to obscure an image are capable of being removed. There were however particles remaining on the slide. They do not have an effect on the clarity of the image in this case, but could impact the quality of an image with a larger focal length.

To determine the smallest particle that could be removed from the slide, the glass microspheres were deposited on the slide as before. A 0.003 inch diameter wire was placed on the slide for comparison purposes and the image shown in Figure 4.8 taken. This wire was removed during testing. The image shows that the largest particle on the slide is approximately 150 μm in diameter and the smallest is less than 5 μm.

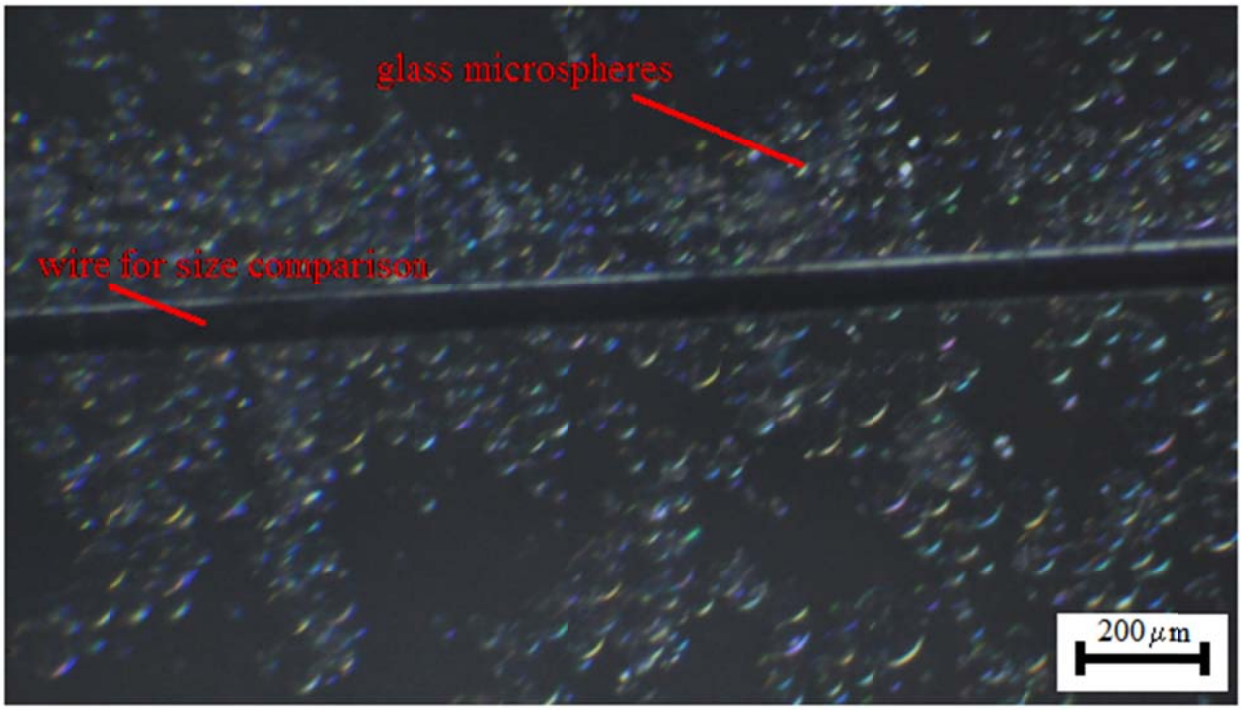


**Figure 4.8: Pre Cleaning**

The slide with the glass microspheres was then excited at 8600 Hz. It was allowed to vibrate until the microspheres could no longer be seen falling from the surface, approximately 10 seconds. Figure 4.9 shows the slide after this test. The largest particles have been removed as have the bulk of the deposited particles. One observation that can be made is that the remaining

particles are mostly isolated from one another with some smaller particles grouping around the larger particles. The largest remaining particles are approximately 80 μm in diameter.

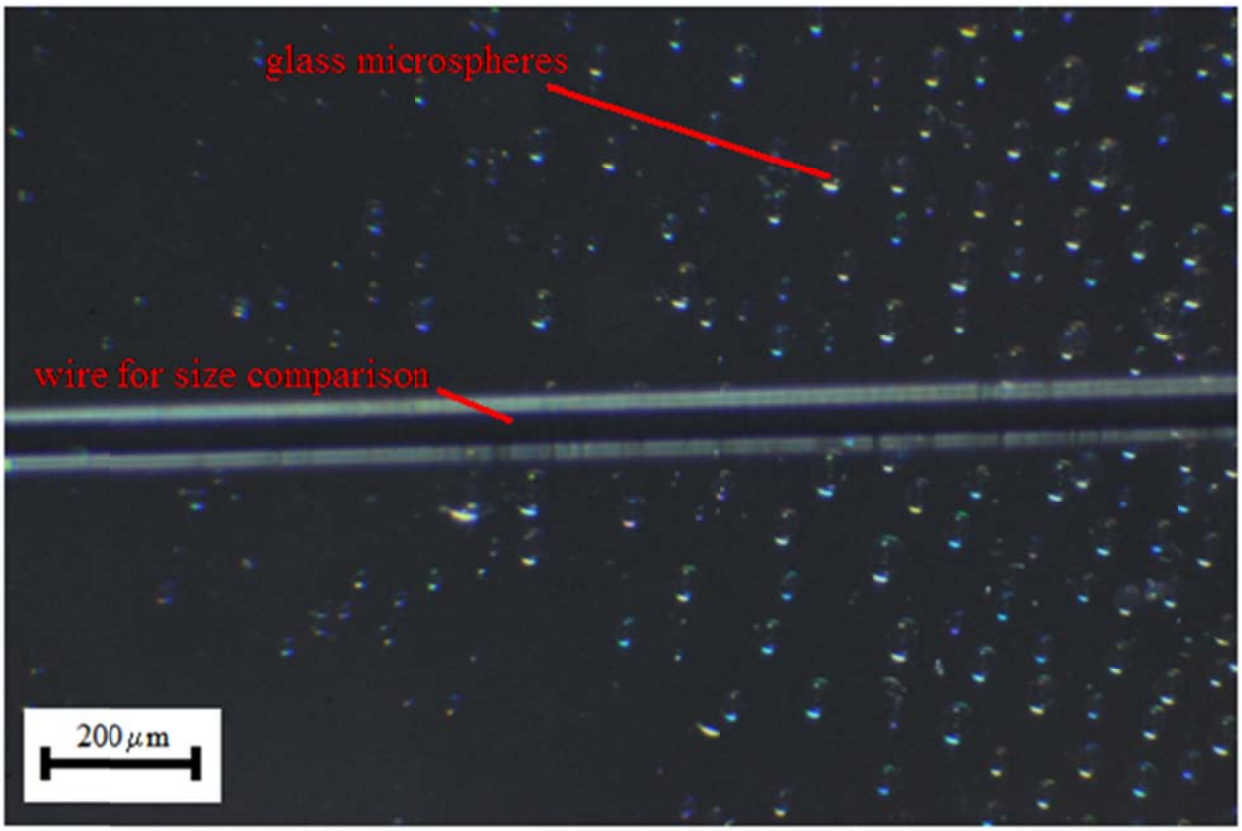


**Figure 4.9: Post Vibration, f = 8600 Hz, Pre Air**

Following the initial test using only vibrations, the slide was placed at the outlet of the small wind tunnel described in Chapter 3. The wind tunnel was then turned on and allowed to run for 20 seconds at a velocity of 3.5 m/sec. The slide was not excited during this test.

Figure 4.10 shows the slide after the test using airflow with no vibrations. The largest particle remaining is approximately 40 μm in diameter so some particles were removed which remained after the vibration only test. Perhaps the most important observation for this test is in the comparison of the distribution of the particles over the surface with that of Figure 4.9. In the

previous figure, the particles were mostly isolated from one another with only smaller particles adjacent to the large particles. In Figure 4.10 the particles have been pushed together into clumps.

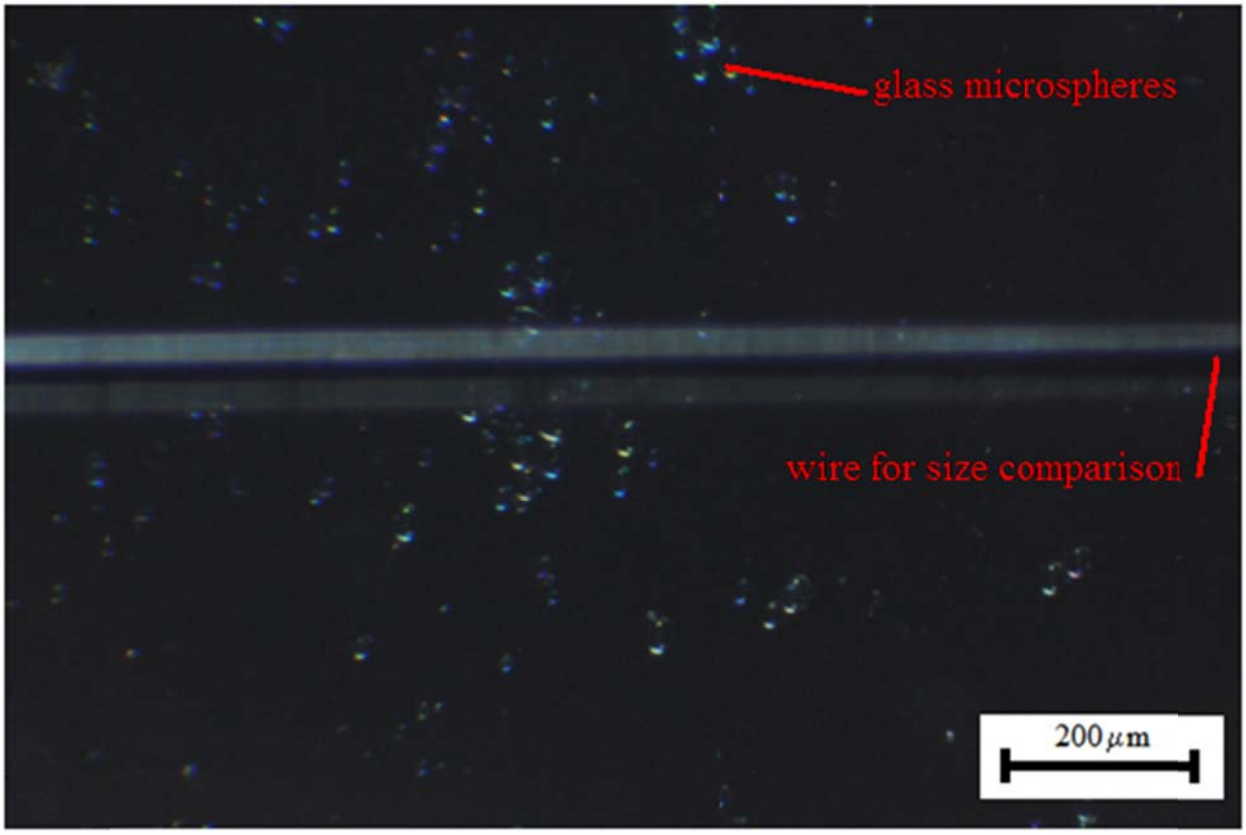


**Figure 4.10: Post Air, u = 3.5 m/s, without Vibrations**

The final test used both the airflow and dynamic excitation of the slide. The airflow velocity was 3.5 m/sec, the frequency of vibration was 8600 Hz and the duration of the test was approximately 20 seconds. The surface of the slide following this test is shown in Figure 4.11. With the exception of one 80 μm diameter particle, the remaining particles are smaller than 5 μm in diameter. When Figure 4.11 is compared with Figure 4.8, it appears that a combination of dynamic excitation and airflow was capable of removing over 99% of the original particles.

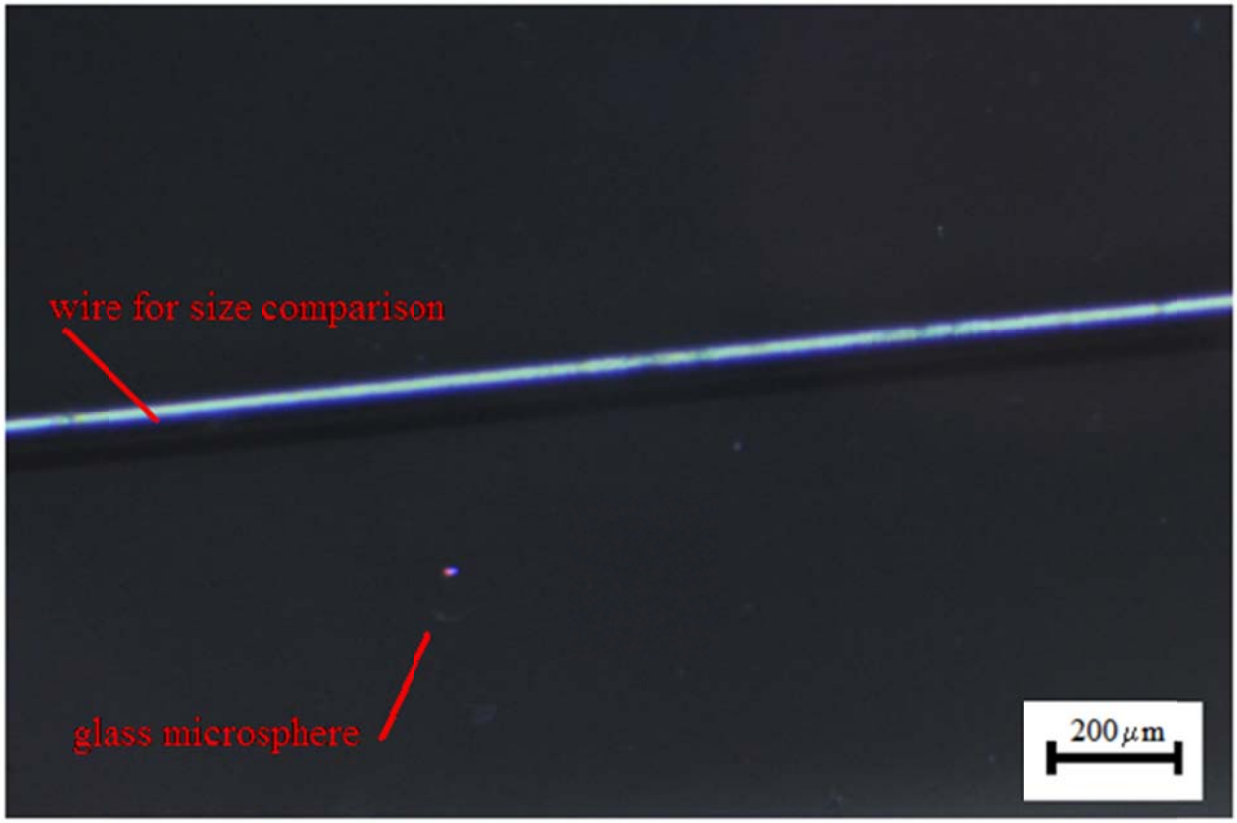


**Figure 4.11: Post Vibration, f = 8600 Hz, and Air, u = 3.5 m/s**

## 4.4 Discussion of Results

The preceding sections clearly show that it is possible to remove particles from a glass surface using remotely commanded dynamic vibrations. There are, however, several points that require more discussion. First of these is the large difference between the theoretical adhesive force and what was calculated based on the experimental evidence. Table 4.5 gives the adhesive forces and removal accelerations for an 80 μm diameter microsphere. The theoretical adhesive force includes the electrostatic forces as well as the Van der Waals force. The Van der Waals force is of the same magnitude as the total adhesive force which indicates that even if there are no electrostatic forces acting on the particle, the predicted adhesive force is still three orders of magnitude larger than was observed.

**Table 4.5: Theoretical and Experimental Adhesive Force for 80 μm Glass Microsphere**

| | Predicted Forces | Observed Forces |
|---|---|---|
| $F_{adh}$ (N) | 7E-06 | 5E-09 |
| $F_{vdw}$ (N) | 4E-06 | 5E-09 |
| a ($m/s^2$) | 1.2E+05 | 1.5E+02 |

diameter = 80 μm

mass (kg) = 3E-11

weight (N) = 3E-10

There are several possible causes of the discrepancy between the theoretical and observed adhesive force including gravity, surface asperities and boundary layer effects. During testing the slide was oriented so that its plane was perpendicular to the ground. In this position, for a particle to slide off of the surface while the slide is vibrating the weight must be greater than the friction force. Equation 32 represents this with the frictional force given by the difference between the adhesion force and the inertial force times the coefficient of static friction.

$$F_w \geq (F_{adh} - F_{int})\mu_{sf} \tag{32}$$

For an 80 μm glass microsphere, Eqn. 32 requires a coefficient of friction on the order of 0.0001 if the particles are to be removed by gravitational forces. For comparison, the lowest measured coefficient of friction for a solid is 0.02[29]. This would indicate that if gravitational forces are influencing particle removal it is not by overcoming the friction between the particle and the surface. What could be happening is that the round microspheres are rolling off of the surface. They may initially be held to the surface because of roughness on the sphere or the surface, or even because of a small deformation[7] in the particle due to the adhesive force. As the surface deflects, the reduced adhesion force allows the microspheres to roll free of the surface.

The second likely cause for the observed adhesive force to be less than the theoretical is because of surface asperities. The equations for the adhesive forces all assume perfectly spherical particles on perfectly flat surfaces. The glass beads used for this research approximate this condition but small surface irregularities could still reduce the observed force. If there are irregular features on the particle or surface, they effectively increase the separation distance, z, between the particle and surface. The Van der Waals force scales with $1/z^2$, as does the image

force. For a single order of magnitude drop in the adhesive force the separation distance only needs to increase to 12 Å from the assumed value of 4 Å. The increased separation distance could also be caused by a film or residue on the surface or particle.

Another possible cause for the lower observed adhesion force is due to the formation of a boundary layer on the slide surface. At the surface of a vibrating structure, the air moves exactly with the surface which results in a zero relative gas velocity normal to the surface. For small particles this layer may be thick enough to envelope the entire particle and drag it along with the surface. For larger particles though, this boundary layer could act as a cushion between the particle and surface. If a particle were to attain a slight separation distance without actually escaping the surface, the boundary layer would slow the movement of the particle as it was re-attracted to the surface and thereby reduce the adhesive force.

In summary, the difference between the theoretical adhesion force for an 80 μm microsphere (7000 nN) and the observed adhesion force (5 nN) is mainly due to surface roughness. The weight of the microspheres (0.3 nN for d = 80 μm) is not sufficient to account for a significant reduction of the adhesive force, and the proposed boundary layer influence cannot be credited with reducing the adhesion force as it was not physically observed. That being said, clearly there is something that is reducing the observed adhesion force in addition to surface roughness on the microspheres and glass slide.

In addition to the assumption of perfect spheres and planes, the theoretical adhesive force equations assume that there is only a single particle interacting with the plane. When Figure 4.9 is considered, the ordered distribution of the particles across the surface indicates that the particles adhere to one another as well to create larger agglomerations of particles. This grouping of particles could behave as a single large particle allowing for smaller particles to be removed. The converse of this is possibly the case after airflow is applied without vibrations. In Figure 4.10 the particles appear to be bunched into groups again which would indicate that drag

forces on the particles are working to remove them. The drag forces cease to be effective when the grouping of particles causes the friction forces to exceed the drag forces. This occurs as the groups grow because each additional particle contributes to the friction force, while particles in the center or leeward side of the group experience less drag force than those on the windward side. This is another important observation, specifically that a single particle can cause groups of particles to gather together. Each individual particle may not influence image quality, but as a group they may block enough light adversely influence an image.

The image showing particles after a combination of vibrations and airflow indicates that by combining the airflow and vibrations, nearly all of the particles which were present on the slide were successfully removed. It is proposed that the mechanism by which the remaining particles were removed is a combination of inertial forces and drag forces. The best explanation for the particles removal is that the surface accelerations reduce the adhesive force sufficiently to allow the drag forces to displace the particles. Once the particles are moving along the surface they can either be pushed entirely from the surface or forced to agglomerate into a larger mass and then knocked free.

# 5. Conclusions and Recommendations

## 5.1 Conclusions

Based upon the results of this research, a dynamic cleaning system which uses structural vibrations and a gas flow to remove particles is possible. Depending upon the application, gas flow may not be required. For example, the particles (d~ 100 to 250 μm) which were of concern in the MER DIMES system described in Chapter 1 could be removed using a system such as this with only structural vibrations.

The experimentally observed adhesion force is approximately three orders of magnitude less than the theoretically predicted adhesion force. The reason for this discrepancy is attributed to the surface roughness of the particles and glass slide. An additional reason for the lower observed adhesion force is due to the interaction of the particles themselves. Particle to particle attractions would create larger groups which act as single particles, and particle to particle collisions could increase the ability of particles to be removed.

## 5.2 Recommendations

This author recommends that for future work a commercial camera lens or filter be obtained. The experimental device used for this research was sufficient to show that particles could be removed from a glass surface, but does not lend itself well to integration into an optical system. Additionally, if a camera lens were used the effect of the boundary conditions on the surface accelerations of the glass could be investigated.

Another consideration to be investigated in the future is the disposition of the exciting elements of the device. It is recommended that a washer shaped stack actuator be obtained which matches the circumference of a circular lens. This configuration could be compared to one which used a number of individual stack actuators spaced around the circumference of the lens. The purpose of spacing individual actuators around the lens would be to determine if a lower operating

voltage could be used by operating the actuators out of phase with one another. This would require determining the mode shape of the lens at an individual frequency and placing the actuators at the anti-nodal lines. This setup would be significantly more complicated than a single circular actuator, or even operating the multiple actuators in phase, but could reduce the power requirements.

During testing for this work, the particles were immediately removed after being deposited. There is however a potential for increased adhesion force if the particles are left on the surface for a length of time. The increased adhesion force arises from the deformation of the particles where they become flattened at the interface between the particle and the surface. If this increased adhesion force could not be overcome by the dynamic cleaning system, it would be important to develop a maximum time between particle deposition and cleaning to ensure removal of the particles.

The particles used for this research are of low density and spherical in shape. A particle from the moon's surface for example would have an irregular shape which would tend to decrease the adhesive force. It is recommended that in future works the effect of irregular particle geometry on adhesion force be investigated. The extent to which the force is reduced would reduce the required power for the rejection system and thereby reduce its cost. Also of importance would be an investigation into how vacuum and low gravity influences the behavior of a particle adhered to a surface. For this research, a vacuum test was not performed and the aerodynamic behavior of the particles could only be inferred. Video from the side of the slide during operation was captured, however the magnification of the lens used was not enough to capture the movement of individual particles. For future research, this author also recommends that a higher magnification lens be obtained, or that a different type of assembly be built that could fit under a microscope. The dynamic behavior of the particles on the slide could provide valuable insight into the true nature of the adhesive forces.

For future work there is one thing in particular which needs to be adjusted from this work. That is the amplification equipment used. For this work, the amplifier was sufficient to remove particles but difficult to work with. At high frequencies it had a tendency to short out and become inoperable. Once this problem is corrected, the effectiveness of this system at higher frequencies could be determined.

The final recommendation for future work is to build a cleaning system and integrate it into a camera system. Doing so has two goals, the first of which is to ensure that a system could be built into an optical device while maintaining a separation between the interior of the device and the environment. The method of cleaning a lens proposed in this work would be irrelevant if it allowed particles to enter the camera and settle on elements behind the dynamically cleaned lens. The second goal would be to determine under what circumstances particles influence image quality.

## 6. References


1. Bennet, J. "Contamination on Optical Surfaces – Concerns, Prevention, Detection, and Removal," *Particles on Surfaces 4: detection, adhesion, and removal*, Marcel Dekker, New York, New York, 1995, pp. 101-108.
2. Wilson, R., Mainmone, M., "An Optical Model For Image Artifacts Produced By Dust Particles On Lenses," *Proceedings ISAIRAIS 2005 Conference*, Munich, Germany, 2005.
3. Taylor, L., Schmitt, H., "The Lunar Dust Problem," *1st Space Exploration Conference: Continuing the Voyage of Discovery*, Orlando, Florida, United States, 2005.
4. Walton, O., "Adhesion of Lunar Dust," NASA/CR-2007-214685, April 2007.
5. Brereton, G., Qi, Q., "Mechanisms of Removal of Micron-Sized Particles by High-Frequency Ultrasonic Waves," *IEEE Transactions on Ultrasonics, Ferroelectrics, and Frequency Control*, Vol. 42, No. 4, July 1995, pp. 619-629.
6. Bowling, R., "An Analysis of Particle Adhesion on Semiconductor Surfaces," *Journal of the Electrochemical Society, Solid State Science and Technology*, Vol. 132, No. 9, April 1985, pp. 2208-2214.
7. Krupp, H., Sperling, G., "Theory of Adhesion of Small Particles," *Journal of Applied Physics*, Vol. 37, No. 11, October 1966.
8. Ranade, M.B., "Adhesion and Removal of Fine Particles on Surfaces," *Aerosol Science and Technology*, January 1987, pp. 161-176.
9. Jones, R., Pollock, H., "Adhesion Forces Between Glass and Silicon Surfaces in Air Studied by AFM: Effects of Relative Humidity, Particle Size, Roughness, and Surface Treatment," *Langmuir, The ACS Journal of Surfaces and Colloids*, Vol. 18, No. 21, 2002, pp. 8045-8055.
10. Walton, O., "Review of Adhesion Fundamentals for Micron Scale Particles," *KONA Powder and Particle Journal,* No. 26, 2008, pp. 129-135.
11. Ackler, H., French, R., Chiang, Y., "Comparisons of Hamaker Constants for Ceramics Systems with Intervening Vacuum or Water: From Force Laws and Physical Properties," *Journal of Colloid and Interface Science* **179**, Article No. 0238, 1996.

12. Busnaina, A., Gale, G., "Ultrasonic and Megasonic Particle Removal," *Precision Cleaning Proceedings*, Chicago, IL, 2005, pp. 347-360.
13. Tan, M., Friend, J., Yeo, L., "Direct Visualization of Surface Acoustic Waves Along Substrates Using Smoke Particles," *Applied Physics Letters* **91**, 224101, 2007.
14. Lederer, P., "Piezoelectric Shakers And How They Are Used," *Noise & Vibration Control Worldwide*, Vol. 18, No. 6, 1987.
15. Zamfir, A., Drimbarean, A., "An Optic Model of the Appearance of Blemishes in Digital Photographs," *Proceedings of the SPIE Digital Photography III*, Vol. 6502, 2007.
16. Hogan, T., "Cleaning Your Sensor," www.bythom.co/cleaning.htm, Feb. 2, 2010.
17. Takizawa, H., Kawai, S., U.S. Patent for "Camera and Image Pick-Up Device Unit Having An Optical Member That Is Vibrated To Remove Dust," No. 7,280,145 B2, Issued Oct. 9, 2007.
18. Kawai, S., U.S. Patent for "Dust Removal Camera," No. 7,724,299 B2, Issued May 25, 2010.
19. Barrett, R., Cravens, S., "Infra-through-ultrasonic Cleaning of Microanemometer and Acoustic Vector Sensing Elements," *Proceedings of Active and Passive Smart Structures and Integrated Systems,* San Diego, California, Unites States, 2010.
20. Inman, D., *Engineering Vibration Third Edition*, Pearson Prentice Hall, Upper Saddle River, NJ, 2007, pp. 465-510.
21. Meirovitch, L., *Analytical Methods in Vibrations*, The Macmillan Company, London, 1967, pp. 179-189.
22. Barrett, R., "Intelligent Rotor Blade and Structures Development Using Directionally Attached Piezoelectric Crystals," *Master's thesis*, University of Maryland, College Park, MD, 1990. Bell, T., "Lunar Dust Buster," *NASA Science: Science News*, http://science.nasa.gov/ science-news/science-at-nasa/2006/19apr_dustbuster/, Aug. 8, 2011.
23. Anon., "96% Silica Glass Properties," *Material Properties Data*, matweb.com, October, 2010.
24. Anon., "Low Voltage Piezoelectric Stacks," *Piezo Systems Inc.*, Catalog #7C (2008), Woburn, Massachusetts, United States, pp. 54-55.

25. Anon., “Piezo Linear Amplifier,” *Piezo Systems Inc.*, Catalog #7C (2008), Woburn, Massachusetts, United States, pp. 4-5.
26. Ellison, W., “MOSFET Amplifier Circuit,” The University of Kansas, Dept. of Aerospace Engineering, October, 2010.
27. Anon., “3M Micro-Sphere Selection Guide,” *3M Energy and Advanced Materials Division*, St. Paul, Minnesota, United States, April, 2010.
28. Arai, A., U.S. Patent for “Digital Camera and Cleaning Apparatus Therefor,” No. US 2005/0275738 A1, Issued Dec. 15, 2005.
29. Kleiner, K., “Material Slicker than Teflon Discovered by Accident,” *NewScientist*, http://www.newscientist.com/article/dn16102-material-slicker-than-teflon-discovered-by-accident.html, Aug. 8, 2011.
30. Field, R., U.S. Patent for “Camera,” No. US 2006/0188248 A1, Issued Aug. 24, 2006.
31. Sakurai, M., U.S. Patent Application for “Imaging Apparatus and Dust Reduction Apparatus,” No US 2010/0060760 A1, Pub. Date Mar. 11, 2010.
32. Kawai, S., U.S. Patent Application for “Vibrating Device and Image Equipment Having the Same,” No. US 2010/0158501 A1, Pub. Date Jun. 24, 2010.
33. Watterson, R., Hagemeier, D., U.S. Patent for “Photoelectric Sensor Having Dust Removal Apparatus,” No. 5,879,626, Issued Mar. 9, 1999.